PCCP

Accepted Manuscript

ROYAL SOCIETY OF CHEMISTRY

www.rsc.org/pccp

Enhancement of Electroactive β Phase Crystallization and Dielectric Constant of PVDF by Incorporating GeO_2 and SiO_2 Nanoparticles

Epsita Kar[1], Navonil Bose[1], Sukhen Das[1], Nillohit Mukherjee[2], Sampad Mukherjee[1*]

[1]Department of Physics, Indian Institute of Engineering Science and Technology, Shibpur, Howrah-711103, India

[2]Centre of Excellence for Green Energy and Sensor Systems, Indian Institute of Engineering Science and Technology, Shibpur, Howrah-711103, India

*smukherjee.besu@gmail.com, Ph-+91 9433579392

Abstract

Poly(vinylidene fluoride) (PVDF) nanocomposites are gaining importance in the recent times due to their unique dielectric and electroactive responses. In this work, GeO_2 nanoparticles/PVDF and SiO_2 nanoparticles/PVDF nanocomposite films are prepared by a simple solution casting technique. Surface morphology and structural properties of the as prepared films are studied by X-ray diffraction, scanning electron microscopy, and FT-IR spectroscopy techniques. The studies reveal that the incorporation of GeO_2 or SiO_2 nanoparticles leads to the enhancement of electroactive β phase fraction in PVDF due to the strong interaction in between negatively charged nanoparticle surface and polymer. Thermal properties analyses of the as prepared samples also support the increment of β phase fraction in PVDF. Variation of dielectric constant, dielectric loss, and ac conductivity with frequency and loading fraction of nanoparticles are also studied for all the as prepared films. Dielectric constant of the nanocomposite films increases with increasing nanofillers concentration in PVDF. 15 mass% SiO_2 loaded PVDF film shows highest dielectric constant which can be attributed to smaller size of SiO_2 nanoparticles and the homogeneous, discrete dispersion of SiO_2 nanoparticles in PVDF matrix.

Keywords: PVDF nanocomposites; GeO_2 and SiO_2 nanoparticles; structural properties; phase transformation; dielectric properties.

1. Introduction

Since the last decades, poly(vinylidene fluoride) (PVDF), a flexible, cost effective fluro-polymer has attracted much interest due to their wide range of important technological applications such as high charge storage capacitors, electro-striction for artificial musceles, magnetostriction for nanoparticles, smart skins for drag reduction [1-5]. It has also been used in biotechnology [6], photo recording [7] and microwave modulation [8]. PVDF has been widely investigated because of its unique pyroelectric, piezoelectric, dielectric properties and resistance to chemicals [9-11]. Due to these novel properties, PVDF has promising applications in the area of sensors, actuators, filters, chemical warfare protection, inexpensive strain gauges etc. [12-13].

PVDF ([-CH_2-CF_2-]) is a semicrystalline polymer and posses five different crystalline phases α, β, γ, δ and ε. Out of these phases the non-polar α form is the most thermodynamically stable state at ambient temperature and pressure. α phase most commonly occurs with a dominating fraction in the melt processed PVDF film. The β and γ phases are the polar phases of PVDF, however β phase assumes paramount importance over the other phases due to its better piezo-electric, ferro-electric and pyro-electric properties. The α phase posses TGTG′ (T- trans, G- gauche+, G′-gauche), β phase has all trans (TTT) and the γ phase has 3TG3TG' conformations [14-20]. As a consequence, numerous methods have been developed to enhance the β phase content in PVDF matrix as well as the dielectric properties of PVDF by incorporating different fillers in neat PVDF matrix such as $BaTiO_3$ [21], hydrate ionic salts [22], clays [20,23-25] and rare earth salts [26-28], to name a few. Adding of sub-micron and nano sized fillers into the polymer matrices can improve electrical, mechanical, thermal and magnetic properties significantly. Polymer structure and properties of these polymer nanocomposites are modified due to the formation of interface at the boundary

matrix/fine filler particles and the interphase interactions [29-30]. Ferrite nanocmaterials [31], carbon nanotubes [32], submicron Ni powder [33], TiO_2 nanoparticles [13], copper nanowires [34] are used as the fillers in PVDF matrix to synthesize various PVDF nanocmposites. Incorporation of inorganic semiconductor nanofillers in PVDF matrix can improve the dielectric properties of the nanocomposites significantly without losing flexibility and homogeneity of the synthesized films. P. Indra Devi et al. has reported the enhancement of the dielectric constant of PVDF by incorporated different nanostructured lead sulfide (PbS) as filler [12]. Works has been reported on semiconductor oxide SiO_2 as filler in PVDF for the waste water managment [35], improvement of the performance of the PVDF membranes [36], in Li-ion batteries [37]. Thenganathen et al. [38] have reported the effect of silica (SiO_2) and phosphorus pentoxide (P_2O_5) on the structural, thermal and electrical conductivity properties of SiO_2-P_2O_5-PVDF composites. Though several works have been performed by using SiO_2 as filler in the PVDF matrix but as per our knowledge is concern no such study on the dielectric properties and the nucleation of the β phase has been reported till date by using SiO_2 nanofiller. Again, germanium oxide (GeO_2), a glass semiconductor oxide posses good dielectric [39] and piezo-electric [40] properties, thus the detail study of electrical properties of GeO_2 nanofiller incorporated PVDF will be quite interesting.

The present work is concerned with the incorporation of GeO_2 and SiO_2 nanoparticles (NPs) in the PVDF matrix. We have studied the effect of GeO_2 and SiO_2 NPs on the nucleation of the electroactive β phase as well as enhancement of the dielectric properties of the as synthesized PVDF nanocomposites films. Surface morphology, thermal and electrical properties of the GeO_2 NPs/PVDF and SiO_2 NPs/PVDF nanocomposite films are also studied in this work.

2. Experimental

2.1 Materials

Poly(vinylidene fluoride) (PVDF) pallets with molecular weight 275000 are obtained from Aldrich,USA. Dry N,N, dimethylformamide (DMF, Merck, India), germanium oxide (Alfa Aesar, 99.99%), tetraethyl orthosilicate (TEOS, Merck, Schuchardt) ethanol (Merck, Germany) and aqueous ammonia (strength 30%, Merck, Germany) are used in this work. All the materials were used as received.

2.2 Synthesis of GeO_2 and SiO_2 NPs

GeO_2 NPs are synthesized by typical hydrothermal method [39] taking GeO_2 powder as the starting material. At first a stock solution of GeO_2 with sparingly hot water is prepared. Then a required amount of solution is taken in a properly sealed stainless steel autoclave which is heated at 185°C for 24 hrs in a furnace. Then the autoclave is set for natural cooling. After cooling down to room temperature (30°C), the water is being evaporated to collect the GeO_2 NPs.

The SiO_2 NPs are synthesized by the modified Stöber's method [41]. In this typical preparation technique, first a mixture of 160 ml ethanol, 40 ml distilled water and 5 ml of ammonia is prepared by vigorous stirring for 30 min. Then 2 ml of TEOS is slowly added into the resulting mixture which is stirred for 12 hrs by using a magnetic stirrer at room temperature (30°C) and the resulting solution is dried to obtain SiO_2 NPs.

2.3 Synthesis of GeO_2 /PVDF and SiO_2/PVDF nanocomposite films

The semiconductor oxide PVDF nanocomposite films (SPN films) are synthesized by the simple solution-casting method. In a typical synthesis procedure, 200 mg of PVDF is dissolved in 5 ml DMF under magnetic stirring at 60°C and the complete dissolution of

PVDF in DMF is achieved. Then a certain mass percentage of both the NPs (5-15 mass%) are added in the solution of PVDF and vigorously stirred for 12 hrs followed by 30 min of ultrasonication. The SPN films are obtained by casting the whole mixture in a properly cleaned and dried Petri dish and evaporating the solvent at 90°C. Neat PVDF films are also prepared following the same procedure along with the loaded PVDF films. The thicknesses of the as synthesized neat PVDF and SPN films, as measured by digital micrometer (resolution: 10^{-3} mm) are ~ 100±5 μm. The details of the as synthesized samples are given in the Table-1.

2.3 Characterization

The structural properties of the as synthesized films are studied by using X-ray diffractometer (Bruker-D8) with Cu-Kα radiation (wavelength 1.541 Å), Bragg-Brentano goniometer geometry and θ-2θ scanning mechanism. To have an idea about the thermal properties of the samples, differential thermal analysis (DTA) and thermo gravimetric analysis (TGA) are performed by using TGA/SDTA851 Mettler Toledo apparatus in air atmosphere at a heating rate of 10 °C/min. Vibrational spectra for all the samples are recorded at room temperature by the Fourier transform infrared (FTIR) spectroscope (Jasco FT/IR-460 PLUS) with a resolution of 1 cm^{-1}. The fraction of β phase F(β) in the as synthesized SPN films is calculated from the FT-IR spectra using Lambert-Beer law as given by [42],

$$F(\beta) = \frac{A_\beta}{\left(\frac{K_\beta}{K_\alpha}\right) A_\alpha + A_\beta} \quad (1)$$

Where A_α and A_β are the absorbance at 764 cm^{-1} and 840 cm^{-1} respectively, K_α ($6.1\times10^4 cm^2 mol^{-1}$) and K_β(7.7×10^4 $cm^2 mol^{-1}$) are the absorption coefficients at the respective wave numbers [42]. The surface morphology of the NPs and the nanocomposite PVDF films are studied by using field emission scanning electron microscopy (FESEM) (FEI, INSPECT F50) technique. The as synthesized nanoparticles are also characterized by scanning electron

microscopy (SEM) (Hitachi S3400N) as well as transmission electron microscopy (TEM) (TECNEI) techniques. The dielectric properties of the SPN films were studied using a digital LCR meter (Agilent, E4980A). The value of the dielectric constant (ε′), Dielectric loss (ε′′) and total ac conductivity (σ_{ac}) of the samples are calculated using the following equations,

$$\varepsilon' = \frac{C.d}{\varepsilon_0 A} \quad (2)$$

$$\varepsilon'' = tan\delta.\varepsilon' \quad (3)$$

Where $tan\delta = \frac{\varepsilon''}{\varepsilon'}$

$$\sigma_{ac} = 2\pi f \varepsilon_0 \varepsilon'' \quad (4)$$

Where *C*, d, A and ε'' are the capacitance, thickness, effective area and dielectric loss of the samples respectively. *f* is the frequency of the electric field applied across the samples and ε_0 is the free space permittivity (8.854×10^{-12} F.m^{-1}).

3. Result and discussion

3.1 XRD analysis

Fig.1a shows the XRD patterns of the neat PVDF film (P0) and PVDF films filled with GeO_2 NPs of different concentrations, c.a. PG5, PG10 and PG15. The well recognizable peaks positioned at the 2θ values 26.2°, 38.4°, 40°, 42.2°, 49.1° are clearly indexed to the hexagonal GeO_2 crystalline phase corresponding to the (101), (102), (111) ,(200) and (112) planes (JCPDF-43-1016), that infers the incorporation of GeO_2 NPs in the PVDF polymer matrix. The XRD pattern of the neat PVDF film (P0) reveals the semicrystalline nature with peaks around 2θ values of 17.8°, 18.5°, 20° (characteristic peak) and 26.7° corresponding to the (100), (020), (021) and((201),(310)) planes of α phase PVDF respectively [42]. Another peak

positioned at 38.7° is attributed to the (211) plane of the γ phase of PVDF [20, 42] which is only prominent for P0. The enlarged view of the XRD patterns for the diffraction angle (2θ) range 15° to 25° is shown in Fig.1b. It can be clearly seen from the figure that all the three GeO_2 NPs loaded PVDF samples PG5, PG10 and PG15 exhibit the peak around 2θ≈20.3° (characteristic peak) corresponding to the (110), (200) planes of β-PVDF [42], whereas neat PVDF (P0) shows peak around 20°. However a new prominent peak of β phased PVDF appears at 36.5° ((020) and (101)) [20] for GeO_2 NPs loaded samples as shown in Fig.1a. Another prominent peak emerges at 20.9° with the increase of GeO_2 nanofillers percentage in PVDF, which can be indexed to the (100) plane of the hexagonal GeO_2 crystalline phase (JCPDF-43-1016). XRD patterns of the SiO_2 NPs, neat PVDF film, PS5, PS10 and PS15 are shown in Fig.2a. The figure shows a hump in the lower 2θ region, positioned at ~ 2θ=23° (characteristic peak) for all the SiO_2 NPs incorporated PVDF films, suggesting the successful inclusion of amorphous SiO_2 NPs in PVDF [38]. The enlarged view of the XRD patterns in Fig.2b shows that the loading of SiO_2 NPs also results in a characteristics peak at 2θ = 20.3° which is attributed to the (110),(200) planes of β-PVDF. The position of the amorphous broad hump of the SiO_2 NPs coincides with the 2θ=20.3° which consequences in a masking phenomenon over that region. Thus the appearance of the β-PVDF related peak at 20.3° is not prominently observed for the higher loading concentration of SiO_2 NPs (PS15). As a whole, we can infer from the XRD results that the main peak of α-PVDF at 20° is replaced by the peak positioned at 20.3° with the addition of both the nanofillers, hence it suggests the nucleation of electroactive β phase in the SPN films for different filler concentration.

3.2 Electron microscopic analyses

Fig.3a shows the SEM micrograph of the as synthesized GeO_2 nanoparticles. The size distribution of the GeO_2 nanoparticles as obtained from the SEM micrograph is shown in the inset of the Fig.3a. It is evident from the figure that the GeO_2 nanoparticles have cube like

shape with an average diagonal length of ~ 615 nm. TEM micrograph of the as synthesized GeO_2 nanocrystals is shown in Fig.3b which reveals that GeO_2 nanocrystals having diagonal length in the range 75-175 nm. The inset of the figure shows the size distribution of the as synthesized GeO_2 nanoparticles as obtained from TEM micrograph, which reveals that the nanoparticles have an average diagonal length of ~ 125 nm. The larger size of the GeO_2 nanoparticles as obtained from the SEM analysis is the result of the agglomeration of the nanoparticles in powder form. Low magnification FESEM image of as synthesized SiO_2 NPs is shown in Fig.4a. Surface morphology of the sample in Fig.4a indicates that the particles have spherical shape and the diameter of the SiO_2 NPs are in the range of 90 -160 nm. The figure also depicts that the spherical particles are uniformly dispersed in the entire region. The inset of the figure shows the size distribution of the as synthesized SiO_2 NPs as obtained from the FESEM micrograph, which shows that the nanoparticles have an average diameter of 115 nm. Fig.4b shows typical high magnification FESEM micrograph of SiO_2 NPs indicating the formation of almost mono dispersed nanospheres which are again composed of smaller NPs .TEM micrograph of the SiO_2 NPs is shown in the Fig.4c along with the size distribution (inset) plot of the NPs, which shows that the monodispersed spherical NPs have an average diameter of 42 nm.

Fig.5a, Fig.5b and Fig.5c exhibit the FESEM micrographs of the neat PVDF film, PG15 and PS15 respectively. The neat PVDF film (Fig.5a) shows a highly compact and uniform morphology. In Fig.5b, surface morphology of the GeO_2 NPs/PVDF nanocomposite film reveals the successful inclusion of cube like GeO_2 nanoparticles in PVDF matrix which also leads to a cube like morphology of the composite. A thin layer of polymer can be observed over the embedded GeO_2 particles from Fig.5b. Embedded GeO_2 particles at the surface are relatively larger in size as they are formed by the agglomeration of smaller GeO_2 nanoparticles of average diagonal length 125 nm. Fig.5c shows the surface morphology of the

spherical SiO_2 NPs loaded PVDF film, which reveals the successful inclusion and homogeneous dispersion of spherical SiO_2 NPs in PVDF matrix. Mono dispersed NPs are nicely distributed over the polymer surface without showing any distinct agglomeration. The sizes of the embedded SiO_2 NPs are in the range of 30-50 nm as observed from the Fig.5c. The size distribution of the embedded SiO_2 NPs is also supported by the TEM micrograph of the as synthesized SiO_2 NPs powder in Fig.4c, though the FESEM micrograph of the as synthesized spherical SiO_2 NPs infers the agglomerated particles having larger size (90-160 nm) in Fig.4b. The smaller size distribution of the embedded SiO_2 NPs in PVDF matrix may be originated due to the ultrasonication and continuous stirring of the solution during the synthesis of SiO_2 NPs/ PVDF composites, which provide sufficient energy for separation and forming smaller SiO_2 NPs from agglomerated SiO_2 particles in powder form. The polymer matrix itself also retards the agglomeration process of silica NPs.

3.3 FTIR analysis

The as recorded Fourier transform infrared (FTIR) spectra for the GeO_2 NPs loaded PVDF films and SiO_2 NPs loaded PVDF films are shown in Fig.6a and Fig.7, respectively. Both figures also contain the FTIR spectrum for the as synthesized neat PVDF film (P0). The spectrum of P0 shows characteristic peaks around at 489 cm^{-1} (CF_2 waging), 533 cm^{-1} (CF_2 bending), 615 and 764 cm^{-1} (CF_2 bending and skeletal bending), 796 and 974 cm^{-1} (CH_2 rocking) corresponding to the IR bands of the α-PVDF [20] and two small peaks positioned at 510 cm^{-1} (CF_2 stretching) and at 840 cm^{-1} (CH_2 rocking, CF_2 stretching and skeletal C-C stretching) corresponding to the β-PVDF [20]. However, two new peaks are found to appear at 475 cm^{-1} (CF_2 deformation) and 600 cm^{-1} (CF_2 wag) for both types of SPN films, which are clearly indexed to the β phase of PVDF [20]. In addition, with the 5 mass% loading of GeO_2 and SiO_2 NPs in PVDF matrix the relative intensities of the characteristic peaks of the β-PVDF are significantly improved, in contrast to the decline in the intensities of the

characteristic peaks of the α-PVDF. Fig.6b shows a magnified view of the marked section of Fig.6a in the range of 540 cm^{-1} to 620 cm^{-1} for the samples PG5, PG10 and PG15. Two well defined peaks at 558 cm^{-1} and 586 cm^{-1} related to the O-Ge-O bending vibration of the GeO_2 nanocrystals are observed from the Fig.6b. These characteristic peaks confirm the presence of hexagonal GeO_2 (β phase α-quartz type structure) crystalline phase in the PVDF matrix [43]. For the SiO_2 NPs loaded PVDF films, a well-defined IR absorption related peak is appeared at 1100 cm^{-1} which is assigned to the anti symmetric stretching mode of Si-O-Si group [44]. Thus it confirms the successful inclusion of SiO_2 NPs in the PVDF polymer matrix. As recorded FTIR spectra clearly indicate that mixing a moderate amount of GeO_2 and/or SiO_2 NPs into the PVDF matrix can induce the transformation of the semicrystalline PVDF from the α-phase into the β-phase. β phase PVDF can provide the piezoelectric effect as a result of spontaneous polarization. Therefore, the addition of GeO_2 and/or SiO_2 NPs can improve the piezoelectric property of the PVDF composite films.

The relative fraction of electroactive β phase content F(β) in the NPs loaded PVDF films is calculated using Eqn.(1) . The variation of F(β) (%) as a function of NPs content is shown in the Fig. 8a and Fig.8b for GeO_2 NPs loaded and SiO_2 NPs loaded PVDF films respectively. The β phase fraction for the neat PVDF is and with the loading of GeO_2 nanofiller in PVDF matrix, the fraction of β phase (F(β)) is increased and attains a maximum value (~ 60%) for the nanocomposite film containing 5 mass% GeO_2 NPs . Then it becomes almost saturated for the samples containing higher fraction of GeO_2 nanofiller as shown in Fig.8a. In case of the SiO_2 NPs loaded PVDF films the maximum β phase fraction (F(β)) is obtained for the sample containing 5 mass% SiO_2 NPs, then it decreases for the sample containing 10 mass% SiO_2 NPs and becomes almost saturated. Thus the most intimate interaction between the NPs and the PVDF matrix occurs for 5 mass% nanofiller loaded samples. Similar variation of the β phase fraction (F(β)) for different fillers such as clay [20], Fe_2O_3-Co_3O_4 [45] loaded PVDF

samples has also been reported previously. Thus it can be confirmed from the FTIR spectroscopy that the filler loading accelerate the nucleation as well as stabilization of electroactive β phase in PVDF.

3.4 Thermal analyses

The results of the differential thermal analysis (DTA) and thermo gravimetric analysis (TGA) of sample P0, PG5 and PS5 are shown in Fig.9a, Fig.9b and Fig.9c, respectively. Significant weight loss can be seen from the TGA curve for the sample P0 in Fig.9a, which starts around 450°C and continues upto ~500°C. This phenomenon is related to the decomposition of neat PVDF (P0) followed by the chain stripping mechanism [46] within this temperature range. As a consequence, a well-defined endothermic peak is observed in the DTA curve at 450°C for the sample P0. During this degradation process, about 43.6 % hydrogen fluoride (HF) gas is found to be released from the sample as calculated from the TGA curve[46]. A small endothermic peak around 154°C can also be seen in the DTA curve, which is attributed to the melting temperature of neat PVDF [33]. TGA and DTA analyses are performed for all the three variants of GeO_2 and SiO_2 loaded PVDF films. Since the sample PG5 posses maximum F(β) for the GeO_2 loaded PVDF films as well as TGA and DTA curves of PG5, PG10 and PG15 show almost similar nature, hence only the result corresponding to PG5 is provided here in Fig.9b. For the same reason the TGA and DTA results for PS5 are shown here in Fig.9c. The DTA and TGA curves for the GeO_2 NP incorporated PVDF film (PG5) in Fig.9b depicts that the endothermic peak related to melting temperature in DTA curve is shifted to ~159°C in comparison with neat PVDF (~154°C) which is in fair agreement with the results reported by S. M. Lebedev et al. [33] for the PVDF/nickel composite films where a 5-7°C increase in melting point has been observed after Ni loading (0 to 2.0 wt%). This increase in the melting temperature may be attributed to the change in degree of crystallinity and homogeneity in submolecular structure of the composite film compared to the non-modified

PVDF films [33, 47]. The presence of externally added dopant centers (GeO_2 and SiO_2 NPs) in the polymer matrix is responsible for such changes in the melting region of the SPN films [33, 47]. The increase of the melting temperature of the SPN film also confirms the nucleation of the electroactive β phase in the nanocomposite films [20]. An interesting outcome can also be seen from the DTA and TGA curves for the sample PG5 revealing a decrease in the decomposition temperature which may be occurred due to the agglomeration of the GeO_2 NPs in the PVDF matrix [33]. The starting point of decomposition temperature reduces to ~382°C from 450°C (neat PVDF). Consequently, an endothermic peak is observed at ~385°C. The DTA and TGA curves for PS5 (as shown in Fig.9c) also exhibit an increase of 5°C in melting temperature of the sample compared to that of neat PVDF. However a small decrease in the degradation temperature can be observed from the TGA curve of the SiO_2 NPs loaded sample (PS5) in Fig.9c. The details of the degradation behavior of the neat PVDF and SPN films can be discussed from the DTG curves shown in Fig.10. Maximum degradation temperature (T_{max}),(the temperature at which maximum weight loss rate is reached [48]) can be obtained from the DTG curves. The DTG curve corresponding to PG5 shows significant decrease (77 °C) in T_{max} comparison to that of P0 (462°C). However, T_{max} is slightly shifted about 3-4°C for PS5 (458°C). This decrement of the degradation temperature for PG5 may be attributed to the agglomeration of GeO_2 NPs in PVDF matrix [33]. The result also confirms that the SiO_2 NPs are less agglomerated and comparatively well dispersed in the PVDF matrix than the GeO_2 NPs, which phenomenon is attributed to the smaller size of SiO_2 NPs than that of GeO_2 NPs.

The Coast-Redfern method is generally used to determine the kinetic parameters for thermal degradation of the nanocomposites films [48]. Considering the first order of reaction and random nucleation mechanism, the Coast-Redfern equation can be written as [48],

$$\ln\left(\frac{-\ln(1-\alpha_d)}{T^2}\right) = -\frac{E_d}{RT} + ln\frac{AR}{\beta E_d} \quad (4)$$

Where E_d is the activation energy (here decomposition activation energy), A is the pre-exponential factor, R is the universal gas constant (8.314 J/mol.K), β is the heating rate (10°C/min), T is the degradation temperature (K) and α_d is the degree of conversion. Hence by plotting $\ln\left(\frac{-\ln(1-\alpha_d)}{T^2}\right)$ against 1/T (K^{-1}) a linear trend line can be obtained whose slope gives the value of decomposition activation energy (E_d) of the nanocomposites films. The degree of conversion (α_d) represents the kinetic of conversion of a polymer to volatile decomposition products [48], at a given temperature α_d is defined by [48],

$$\alpha_d = \frac{m_i - m_T}{m_i - m_f} \quad (5)$$

where, m_i, m_T and m_f are the initial sample weight, weight of the sample at temperature T and the final sample weight respectively. In this study, the kinetic parameters of thermal decomposition are evaluated at the vicinity of the maximum degradation temperature (T_{max}) of the sample P0, PG5 and PS5. Fig.11a-c represent the Coats-Redfern plots of the nanocomposites decomposition step of the sample P0, PG5 and PS5 respectively. The regression coefficient (R^2) and estimated activation energy (E_d) values corresponding to the thermal decomposition of the neat PVDF and SPN films for the selected temperature range are tabulated in Table-2. It is worthy to mention that all the linear fitting show regression factor (R^2) values close to unity. The lower value of E_d for the nanocomposite films infers that a less amount of energy is required to remove the volatile decomposition product than P0. The reason behind the lowering of E_d values of the loaded samples is probably due to the sharing of the thermal energy of the loaded nanoparticles with the host matrix. However, the comparative study of E_d value for the sample PG5 and PS5 (as shown in the Fig.10) infers that the sharing of thermal energy with the matrix is more in the case of GeO_2 nanoparticles

than that of the smaller sized SiO_2 NPs. This phenomenon may be attributed to the shapes as well as distribution of the embedded nanoparticles in PVDF matrix.

3.5 Mechanism for the β phase formation

The results of XRD, FTIR and DTA studies of the as synthesized SPN films confirm that the incorporation of GeO_2 and SiO_2 NPs in the PVDF matrix leads to an increase in electroactive β phase fraction. Therefore in this context it is worthwhile to analyze the interaction between the NPs and the polymer which promotes the formation of electroactive β phase. Improvement of the electroactive β phase fraction may be attributed to the strong interactions between the PVDF matrix and embedded NPs [42]. This type of ion-dipole interaction between the PVDF matrix and the loaded ferrite nanoparticles to form the electroactive β phase has also been reported by P. Martin et al. [49]. The functional groups at the surface of the SiO_2 nanospheres are predominantly silanol (Si-OH) or ethoxy ($Si\text{-}OCH_2CH_3$) groups [50-51] as SiO_2 nanospheres are synthesized by modified Stöber's method. These silanol groups of silica NPs generate a negatively charged surface [50-51]. The surfaces of the as synthesized GeO_2 nanocrystals are also negatively charged due to the presence of 2-fold co-ordinated Ge related oxygen deficiency (:Ge=) centers [52] which mainly resides at the surface of the nanocrystals. When the negatively charged NPs are added into PVDF matrix in the solution phase, the NPs will act as the substrate for the formation of electroactive β phase. The positive $-CH_2$ dipoles of PVDF chains experience strong electrostatic interactions with the negatively charged NP surfaces. This interaction leads to the alignment of the stabilized PVDF chains on the surface of the NPs in a longer 'all-trans' (TTT) conformation resulting in the formation of electroactive β phase. Thus the surfaces of the NPs act as the nucleation center for the formation of the β phase. Fig.12 depicts the schematic of the ion-dipole interaction mechanism between the NPs and polymer chains leading to the formation of electroactive β phase. In addition to the formation of the electroactive β phase having 'all-

trans' (TTT) conformation there also exists a probability to obtain the 'TTTGTTTG' or γ phase as observed by A.C.Lopes et.al for aluminosilicate/PVDF composites [53]. γ phase formation may occur due to the gauge effect which may be developed by the easier local internal chain rotation, though no such existence of γ phase has been found from our present experimental observations [20].

The maximum value of β phase fraction as obtained for the GeO_2 NPs loaded PVDF films is about ~ 60% for the sample PG5 (5 mass% loading). However about 65% of β phase fraction is achieved for the SiO_2 NPs loaded PVDF films for the same 5 mass% loading of SiO_2. This difference in the activity to endorse the β phase fraction in PVDF may be readily described by the microstructure of the NPs. Since the size of the SiO_2 NPs is much smaller than that of the GeO_2 NPs, this smaller size of SiO_2 NPs allows a more homogeneous and discrete dispersion of NPs in PVDF polymer matrix as seen from the FESEM image of the composite films (Fig.5b and Fig5c). As a consequence the interfacial area of interaction between the nanofiller and the PVDF matrix increases resulting in a more effective interaction to align the polymer chain in a 'all trans' conformation. This results in a greater fraction of β phase for SiO_2/PVDF composites. So, the discretely distributed small sized spherical SiO_2 nanoparticles act as more suitable substrate for the alignment of 'TTT' conformation than the relatively large cubic shaped GeO_2 nanoparticles.

3.6 Dielectric properties

3.6.1. Dependence of dielectric properties on NPs content:

Fig.13a-c demonstrate the variation of the dielectric constant (ε') and dielectric loss (ε'') as a function of GeO_2 NPs loading in PVDF matrix at 1KHz, 10 KHz and 100 KHz. Similarly Fig.14a-c show the variation dielectric constant (ε') and dielectric loss (ε'') as a function of the SiO_2 NPs loading in PVDF films. The dielectric constant increases almost linearly with

both types of NPs loading in PVDF matrix at lower (1 KHz) as well as higher frequencies ($\geq$ 10 KHz). The variations at higher frequency also describe the fact that the loaded PVDF films exhibit higher value of the dielectric constant than that of the neat PVDF even at frequencies $\geq$ 10 KHz. Maximum value of the dielectric constant ~ 18.3 is obtained for the samples PG15 (15 mass% loading) at 1 KHz for the GeO_2 NPs loaded films. For the SiO_2 NPs loaded PVDF films the maximum dielectric constant is found ~30 at 1 KHz for the sample PS15 (15 mass% loading). The variation of the dielectric loss with the nanoparticle loading shows a similar nature as that of the dielectric constant, i.e. increases almost linearly with the increasing filler loading. An unusual feature can be seen in GeO_2 nanoparticles loaded PVDF films where dielectric constant and dielectric loss for the sample with higher filler fraction loaded PVDF (PG15) show lower values than lower filler fraction loaded PVDF (PG10) at 100 KHz. This phenomenon may be interpreted as the result of phase inversion in the PVDF matrix at higher frequency [20].

Fig.15a and Fig. 15b show dependence of the ac conductivities of the samples on the GeO_2 and SiO_2 loading concentration at 1 KHz. The ac conductivity for both the NPs loaded PVDF films increases linearly with the filler contents due to the enhancement of the dielectric loss.

The enhancement of the dielectric properties with the nanofiller content can be attributed to the Maxwell-Wagner-Seller (MWS) interfacial polarization effect [54]. This phenomenon is occurred due to the accumulation of charges at the interfaces in between different phases of the heterogeneous medium consisted with different permittivity and conductivity. At low nanoparticle concentration the NPs are well separated and more discreetly distributed in the polymer matrix. As a consequence, the effective interfacial interaction between the different phases of the SPN films is less. However, with the increasing filler content the number of NPs per unit volume increases resulting in an increased interfacial area while the interparticle distance decreases. This improves the charge accumulation as well as effective interfacial

polarization which results in a higher value of the dielectric constant. This is the reason for the enhancement of the dielectric constant with the filler loading. In addition to the interfacial polarization, the electroactive β phase content in the polymer composites also plays a significant role for the improvement of the dielectric constant at a lower filler loading (≤ 5 mass%). As seen from the Fig.12 the strong dipole interaction between the negatively charged surface of the NPs and the -CH2- group of PVDF also contributes partially towards the enhancement of the dielectric constant by improving polarization at the interfaces between the NPs and electroactive phases of PVDF. Again as the Fig.8a and Fig.8b reveal that the electroactive β phase fraction become almost saturated for the higher mass percentage (>5 mass%) thus the interfacial polarization becomes predominant for the higher GeO_2 and SiO_2 loading and contribute towards the increment of the dielectric constant.

The dissimilarity between the maximum value of the dielectric constant of the two NPs loaded PVDF films (about ~ 18.3 for the GeO_2 loaded PVDF and ~30 for the SiO_2 NPs loaded PVDF films at 1 KHz) is also observed form the Fig.13a and Fig.14a. This observed dissimilarity can be explained by the microstructure of the NPs. As seen from the TEM micrographs of the as synthesized GeO_2 and SiO_2 nanoparticles (Fig.3b and Fig.4c), the average size of the spherical SiO_2 nanoparticles (~42 nm) is much smaller than the cubic GeO_2 nanoparticles (~125 nm). This smaller size of the SiO_2 nanoparticles leads to a more homogeneous and discrete distribution of the NPs in the PVDF matrix than that of the GeO_2 NPs which can be clearly seen from the FESEM images of the sample PS15 and PG15 (Fig.5b and Fig.5c). As a consequence the number of discretely distributed SiO_2 NPs in the polymer matrix is higher than that of the GeO_2 NPs for the same mass percentage. This results in a greater accumulation of charges at the SiO_2/PVDF interface than that of the GeO_2/PVDF, which leads towards the higher value dielectric constant at same filler concentration. The dielectric constant for the sample PG15 is about two times and for PS15 is

about three times higher than that of the neat PVDF at 1 KHz. In fact, larger dielectric constant is advantageous for energy density ($\eta=\varepsilon'\varepsilon_0E^2/2$, where E is the applied field) stored in a capacitor. For instance to generate an energy density of 0.1 J/cm^3 (value for the high performing piezoelectric ceramics), considering 50% conversion efficiency the required electric field for capacitor with neat PVDF ($\varepsilon' \sim 10$) is 47.5 MV/m. Since the dielectric constants of PG15 ($\varepsilon' \sim 18.3$) and PS15 ($\varepsilon' \sim 30$) are higher than neat PVDF, the required electric fields to obtain an energy density 0.1 J/cm^3 are 35.1 MV/m and 27.3 MV/m respectively. Thus for the nanocomposite films a lower electric field is needed to reach the required energy density.

3.6.2 Frequency dependence of the dielectric properties:

Fig.16a and Fig.16b demonstrate the frequency dependence of dielectric constant (ε') of GeO_2-PVDF nanocomposites and SiO_2-PVDF nanocomposites films respectively for different loading concentrations at room temperature and atmospheric pressure. It can be seen from the figures that the dielectric constant decreases with increasing frequency for the neat PVDF (P0) as well as GeO_2 and SiO_2 NPs incorporated PVDF films. This phenomenon may be assigned to the decreasing number of aligned dipoles per unit volume with increasing frequency [55]. The nature of the variation of dielectric permittivity is related to the oscillating free dipoles in an alternating field. At very low frequency ($\omega \ll \frac{1}{\tau}$) where τ is the relaxation time, the orientation of the dipoles follow the field. As the frequency of the external field increases ($\omega < \frac{1}{\tau}$) the dipoles begin to lag the field and the dielectric constant slightly decreases upto the characteristic value ($\omega = \frac{1}{\tau}$) where, the dielectric constant exhibits relaxation process. At very high frequency ($\omega \gg \frac{1}{\tau}$) the dipoles can no longer follow the field and the dielectric constant decreases. Figures also depict that with increasing nanofiller fraction, the dielectric constant of the composite films is also increased at low frequency

region (50 Hz to 10 KHz). The higher value of the dielectric constant at low frequency region may be attributed to the Maxwell-Wagner-Seller (MWS) interfacial polarization effect [54] which appears in the heterogeneous medium consisting of phases with different permittivity and conductivity. On the application of the external electric field space charges are being accumulated at the interfaces of NPs and PVDF matrix itself, which leads to a short range dipole-dipole interaction. This results in a higher value of the dielectric constant at low frequency for the nanofiller loaded films with comparison to the neat PVDF. In addition to that the large surface to volume ratio of the loaded NPs increases the effective interaction between the NPs and the polymer matrix. The decrease of the dielectric constant with the increasing frequency can also be described by the interfacial polarization. Since the interfacial polarization occurs due to the confinement of the charge carrier at the interface, so their movement and accumulation needs a relatively long time results in the decrease in the dielectric constant with frequency [56]. The frequency dependence of the dielectric loss (ε'') of the as synthesized GeO_2 NPs and SiO_2 NPs loaded PVDF nanocomposites films are shown in the Fig.17a and Fig.17b respectively. Both the figures reveal that the dielectric loss of neat PVDF (P0) as well as GeO_2 or SiO_2 NPs loaded SPN films undergo a relaxation process in the frequency range 10^4 Hz to 10^5 Hz. This relaxation process can be attributed to the α_c relaxation [13]. The nature of this relaxation is associated with the molecular motion in crystalline region of the semi-crystalline PVDF. Several, imperfections in crystalline region including chain loops at the lamellar surfaces, chain rotation and twisting at the boundary of the crystal region, discontinuous defects to act as the origin of this type of relaxation [57-60]. The variation of tanδ as a function of frequency is depicted in the Fig.18a and Fig.18b for the GeO_2 and SiO_2 loaded PVDF films for the frequency range 40 Hz to 1 KHz obtained under same conditions. The variation of tanδ with frequency shows a decrease in tanδ with frequency with the maximum value lies near about 0.1 at 1 KHz. The maximum values of

tanδ obtained for the samples PG15 are ~ 0.62 and ~ 1.87 for 10 KHz and 100 KHz respectively. On the other hand the values at 10 KHz and 100 KHz for the sample PS15 are ~ 0.28 and ~1.13 respectively.

Fig.19a and Fig.19b demonstrate the frequency dependence total ac conductivity of the as synthesized GeO_2 NPs/PVDF and SiO_2 NPs/PVDF SPN films respectively at room temperature. The conductivity of the samples can be divided into two parts, at low frequency region the dc conductivity part is dominating but at the higher frequencies the conductivity is being characterized by the frequency dependent conductivity i.e. ac conductivity. The nature of variation of the ac conductivity with frequency also follows the MWS interfacial polarization phenomenon and dielectric relaxation [54]. Thus the ac conductivity increases with the increasing frequency. The highest ac conductivity at 1 KHz has observed for the sample PS15 (~ 1.06×10^7 S/m) and for PG15 (~1.404×10^7 S/m) for the nanocomposites films.

4. Conclusion:

In this work, series of SiO_2 and GeO_2 nanoparticles loaded PVDF nanocomposites films are synthesized by simple solution casting method. Cube like GeO_2 NPs are synthesized by hydrothermal method and spherical SiO_2 NPs are synthesized by modified Stöber's method. XRD results of the as synthesized GeO_2 NP and SiO_2 NP loaded PVDF films indicate the nucleation of β phase PVDF when GeO_2 and SiO_2 NPs are loaded in PVDF matrix. The FESEM micrographs of SPN films reveal the successful inclusion of the NPs in the PVDF matrix. The FESEM micrographs also show that the smaller SiO_2 NPs are more homogeneously dispersed in the PVDF matrix than GeO_2 NPs. However, the SiO_2 NPs are less agglomerated than the GeO_2 NPs in the PVDF matrix. The FTIR spectra of both type of SPN films confirm the enhancement of β phase fraction in SPN films. The nucleation of β

phase in SPN films is attributed to the interactions in between the negatively charged surfaces of the NPs and the positive charge density of the $–CH_2$ group of PVDF, though the most intimate interaction in between PVDF and the NPs occurs at 5 mass% for both type of fillers. The value of the β phase fraction as obtained for the SiO_2 NPs/PVDF films is ~ 65% for 5 mass% loading, whereas 60% F(β) is obtained for GeO_2-PVDF films for the same loading concentration. The higher β phase fraction of SiO_2 NPs/PVDF films may be attributed to the smaller size of SiO_2 NPs than the GeO_2 NPs which lead to a less agglomeration and more homogeneous distribution in the PVDF matrix. The DTA and TGA curves of the NPs loaded samples show an increase in the melting temperature of the SPN films in comparison to neat PVDF which also confirms the increment in the β phase fraction. The enhancement of dielectric permittivity (ε′) for SPN films is evident from the dielectric properties studies. PS15 posses highest dielectric constant among all the studied samples, which is almost three times higher than that of neat PVDF at same frequency. Larger interfacial interaction between the SiO_2 NPs and PVDF matrix is responsible for the higher dielectric constant value of SiO_2 NPs/PVDF films in comparison with the GeO_2 NPs/PVDF films. Thus as a whole, the loading of GeO_2 and SiO_2 NPs in PVDF matrix results alignment of the polymer in long 'all trans' conformation to increase the electroactive β phase fraction which in turn enhances the piezoelectric property of the PVDF nanocomposite films without losing the flexibility. It should be noted that GeO_2 and SiO_2 are abundant in nature and synthesis of these NPs are easy and cost effective. SPN films can provide a higher value of dielectric constant as well. As synthesized SPN films with improved piezoelectric and dielectric properties may be used in future smart electrical devices.

Acknowledgement

One of the author is thankful to INSPIRE, DST, Govt. of India (IF-140209) for providing partial financial support.

References:

[1] 1 Q. M. Zhang, V. Bharti, and X. Zhao, *Science*, 1998, **280**, 2101.

[2] Q. M. Zhang, H. F. Li, M. Poh, H. S. Xu, Z.-Y. Cheng, F. Xia, and C. Huang, *Nature London,* 2002, **419**, 284.

[3] Z. M. Dang, C. W. Nan, D. Xie, Y. H. Zhang, and S. C. Tjong, *Appl. Phys. Lett.* , 2004, **85**, 97.

[4] P. Martins, M. Silva and S. L. Mendez, *Nanoscale*, 2015, **7**, 9457.

[5] J. Y. Li, *Phys. Rev. Lett.,*2003,**90**, 217601.

[6] L.P. Cheng, D.J. Lin, C.-H. Shih, A.-H. Dwan, C.C. Gryte, *J. Polym. Sci. Part B: Poly. Phys.,* 1999, **37**, 2079.

[7] A.Tawansi, A.H.Oraby, E.Ahmed, E.M.Abdelrazek, M.Abdelaziz, *J.Appl. Polym. Sci.*, 1998,**70**, 1759–1767.

[8] A.Tawansi, M.I.Ayad, E.M.Abdelrazek, *J.Appl.Polym.Sci.*, 1999,**72**,771–781.

[9] W. A. Yee, M. Kotaki, Y. Liu, and X. Lu, *Polymer,* 2007,**48**, 512.

[10] M. Wang, J. H. Shi, K. P. Pramoda, and S. H. Goh, *Nanotechnology,*2007, **18**(23), 235701.

[11] F. He, J. Fan, and S. Lau, *Polym. Test.,* 2008, **27**(8), 964.

[12] P. Indra Devi, M. Sivabharathy and K. Ramachandran, *Optik*, 2013, **124**, 3872–3875.

[13] H. Rekik, Z. Ghallabi, I. Royaud, M. Arous, G. Seytre, G. Boiteux and A. Kallel, *Composites: Part B,* 2013, **45**,1199–1206.

[14] A. J. Lovinger, *Macromolecules*, 1981, **14**(2),322–325.

[15] X. Zhou, B. Chu, B. Neese, M. Lin and Q. M. Zhang, *IEEE Trans. Dielectr. Electr. Insul.*, 2007, **14**(5), 1133–1138.

[16] Y. Lu, J. Claude, B. Neese, Q. M. Zhang and Q. Wang, *J. Am.Chem. Soc.,* 2006, **128**(25), 8120–8121.

[17] N. Karawasa and W. A. Goddard III, *Macromolecules*, 1992, **25**(26), 7268–7281.

[18] A. B. Silva, M. Arjmand, U. Sundararaj and R. E. S. Bretas, *Polymer*, 2014,**55**, 226–234.

[19] V. Tomer, E. Manias and C. A. Randall, *J. Appl. Phys*., 2011,**110**, 044107.

[20] P. Thakur, A. Kool, B. Bagchi, S. Das and P. Nandy, *Appl.Clay. Sci*., 2014,**99**, 149–159.

[21] Z. Dang, D. Xie, and C. Shi, *Appl. phy. Lett*., 2007, **91**, 222902.

[22] M. Benz, W.B. Euler and O.J. Gregory, *Macromolecules*, 2002, **35**, 2682–2688.

[23] T.U. Patro, M.V. Mhalgi, D.V. Khakhar and A. Misra, *Polymer*, 2008,**49**,3486–99.

[24] D. Shah, P. Maiti, E. Gunn, D.F. Schmidt, D.D Jiang, C.A Batt and E.R Giannelis. *Adv. Mater.*, 2004, **16**, 1173–1177.

[25] L. Priya and J.P. Jog, *Journal of Polymer Science Part B:Polymer Physics,* 2002, **40**, 1682–1689.

[26] S. El-Sayed, *Physica B*, 2014, **454**,197–203.

[27] A. Hassen, T. Hanafy, S. El-Sayed, and A. Himanshu, *J. Appl. Phy*., 2011,**110**, 114119.

[28] S. El-Sayed, T. A. Abdel-Baset, and A. Hassen, AIP adv., 2014,**4**, 037114.

[29] T.J. Lewis, *IEEE Trans. Dielect. Electr. Insul*., 1994,**1**, 812–825.

[30] T. Tanaka, *IEEE Trans.Dielect. Electr. Insul*., 2005,**12**, 914–928.

[31] P. Martins, X. Moya, L.C. Phillips, S. Kar-Narayan, N.D. Mathur, and S. Lanceros-Méndez., *J. Phys. D*, 2011, **44**, 4820011-4.

[32] S.Yu, W. Zheng, W. Yu, Y. Zhang, Q. Jiang and Z. Zhao, *Macromolecules,* 2009, **42**, 8870–8874.

[33] S. M. Lebedev, O. S. Gefle and S. N. Tkachenko, J. Electrostat., 2010,**68**,122–127.

[34] A. Silva, M. Arjmand, U. Sundararaj and R. E. S. Bretas, *Polymer*, 2014,**55**, 226-234.

[35] S. Zhang, R. Wang, S. Zhang, G. Li and Y. Zhang, *Chem. Eng. J.*, 2013, **230**, 260-271.

[36] Y. Doi, H. Matsumura, Polyvinylidene fluoride porous membrane and a method for producing the same, U.S. Pat. 5,022,990 (1991).

[37] S. Komaba, N. Yabuuchi, T. Ozeki, Z. J. Han, K. Shimomura, H. Yui,Y. Katayama and T. Miura, *J. Phys. Chem. C*, 2012, **116**,1380–1389.

[38] U. Thanganathan and M. Nogami, *RSC Adv.,* 2012, **2**, 9596–9605.

[39] N.Bose, M. Basu, S Mukherjee, *Mater. Res. Bull.*, 2012,**47**,1368-1373.

[40] D. B. Balitskiœ, O. Yu. Silvestrova, V. S. Balitskiœ, Yu. V. Pisarevskiœ, D. Yu. Pushcharovskiœ, and E. Philippot, Cryst. Reports, 2000, **45**, 145-147.STOTHUR FINKWERNER STOBER, ARTHUR FINK WERNER STOBER, ARTHUR FI

[41] W. Stöber, A. Fink and E. Bhon, *J. Colloid interface Sci.*, 1968, **26**, 62-69.WE

[42] P. Martins, A.C. Lopes and S. Lanceros-Mendez, *Prog. Polym. Sci.*, 2014, **39**, 683–706.

[43] N. Bose, G. S. Taki, M. Basu and S. Mukherjee , *Mater. Res. Express*, 2014, **1**, 045013.

[44] S. Zhang, Y. Zhang, S. Huang, H. Liu and H. Tain, *Chem. Phy. Lett.*, 2010, **498**, 172-177.

[45] P. Thakur, A. Kool, B. Bagchi, S. Das and P. Nandy, *Phys. Chem. Chem. Phys.*, 2015, **17**, 1368—1378.

[46] F. Liu, N.A. Hashim, Y. Liu, M. R. Moghareh Abed and K. Li, *J. Membr. Sci.*, 2011, **375**, 1-27.

[47] V.P. Solomko, Filled Crystalline Polymers. Naukova Dumka, Kiev, 1980.

[48] A. Chafidz, M. Kaavessina, S. Al-Zahrani and M. N. Al-Otaibi, *J. Polym. Res*., 2014, **21** 483.

[49] P. Martins, C.M. Costa, M. Benelmekki, G. Botelhob and S. L.Mendez, *CrystEngComm*., 2012, **14**, 2807.

[50] A.V. Blaaderen and A. Vrij, *J. Colloid Interface Science*, 1993, **156**, 1-18.

[51] S. L. Westcott, S. J. Oldenburg, T. Randall Lee and Naomi J. Halas, *Langmuir*, 1998, **14**, 5396-5401.

[52] L. Armelo, F. Heigl, P .S. G. Kim, R.A. Rosenberg et al., *J. Phys. Chem. C*, 2012, **116**, 14163.

[53] A.C.Lopes, Development of electroactive polymer nanocomposites with porous structured materials, Universidade do Minho, 2013.

[54] A.C.Lopes, C.M.Costa, R. Sabater i Serra, I. C .Neves, J. L. Gomez Ribelles, S. Lanceros-Mendez, Solid State Ionics, 2013, **235**, 42–50.

[55] S. El-Sayed, T. A. Abdel-Baset and A. Hassen, *AIP Adv*., 2014, **4**, 037114.

[56] Y. Li, X. Hung, Z. Hu, P.Jing, S.Li and T.Tanaka, *ACS Appl, Mater. Interfaces*, 011, **3**, 4396-4403.

[57] K. Nakagawa and Y. Ishida, *J Polym Sci Part B: Polym Phys*, 1973, **11**, 2153–71.

[58] J. Mijovic, J. W. Sy and T. K. Kwei, *Macromolecules,*1997, **30**, 3042–3050.

[59] K. Naoki, A. William. Goddard, *Macromolecules*, 1995, **16**, 6765–6772.

[60] M. Arous, I. Ben Amor, A. Kallel, Z. Fakhfakh and G. Perrier, *J. Phys. Chem. Solids*, 2007, **68**, 1405–1414.

List of Figure Captions

Figure 1: (a) XRD histogram of the samples P0, PG5, PG10 and PG15; (b) Enlarged view of XRD histogram (15˚ to 25˚) of the samples P0, PG5, PG10 and PG15.

Figure 2: (a) XRD histogram of SiO_2 NPs, P0, PS5, PS10 and PS15; (b) Enlarged view of XRD histogram (15˚ to 25˚) of P0, PS5, PS10 and PS15.

Figure 3: (a) SEM micrograph of as synthesized GeO_2 nanoparticles. Inset shows the size distribution curve of the GeO_2 nanoparticles; (b) TEM micrograph of the GeO_2 nanoparticles. Inset shows the size distribution curve of the GeO_2 nanoparticles.

Figure 4: (a) Low magnification FESEM micrograph of SiO_2 nanoparticles. Inset shows the size distribution curve; (b) High magnification FESEM micrograph of as synthesized SiO_2 nanoparticles; (c) TEM micrograph of the SiO_2 nanoparticles. Inset shows the size distribution curve.

Figure 5: FESEM micrograph of (a) the sample P0; (b) the sample PG15; and (c) the sample PS15.

Figure 6: (a) FTIR spectra of the samples P0, PG5, PG10 and PG15; (b) Enlarged view of the marked portion of Fig.6a.

Figure 7: FTIR spectra of the samples P0, PS5, PS10 and PS15.

Figure 8: variation of F(β) (β phase fraction) with the filler concentration of (a) GeO_2 nanoparticles; (b) SiO_2 nanoparticles.

Figure 9: TGA and DTA curve of (a) the sample P0; (b) the sample PG5; and (c) the sample PS5. Insets show the enlarged view of the marked section.

Figure 10: DTG curves of the neat PVDF (P0), PG5 and PS5. Inset shows the enlarged view of DTG curve for the sample PG5.

Figure 11: Coats-Redfern plot of (a) P0; (b) PG5; (c) PS5.

Figure 12: Schematic diagram of proposed β phase formation mechanism in SPN films.

Figure 13: Variation of dielectric constant and dielectric loss with loading concentration (mass%) of GeO_2; at (a) 1 KHz, (b) 10 KHz, and (c) 100 KHz.

Figure 14: Variation of dielectric constant and dielectric loss with loading concentration (mass%) of SiO_2 at (a) 1 KHz, (b) 10 KHz and (c) 100 KHz.

Figure 15: Variation of ac conductivity at 1 KHz with (a) GeO_2 loading percentage (mass%); (b) SiO_2 loading percentage (mass%).

Figure 16: Variation of dielectric constant (ε′) with frequency of (a) the samples P0, PG5, PG10 and PG15; (b) the samples P0, PS5, PS10 and PS15.

Figure 17: Variation of dielectric loss (ε′′) with frequency of (a) the samples P0, PG5, PG10 and PG15; (b) the samples P0, PS5, PS10 and PS15.

Figure 18: Variation of tanδ with frequency of (a) the samples P0, PG5, PG10 and PG15; (b) the samples P0, PS5, PS10 and PS15.

Figure 19: Frequency dependence of ac conductivity for (a) the sample P0, PG5, PG10 and PG15; (b) the sample P0, PS5, PS10 and PS15.

Table-1. *Details of the composition of the as synthesized PVDF nanocomposite films.*

Name of the sample	Type of the semiconductor oxide	Percentage of semiconductor oxides (mass%)
P0		0
PG5	GeO_2 nanoparticles	5
PG10		10
PG15		15
PS5	SiO_2 nanoparticles	5
PS10		10
PS15		15

Table-2. *Activation energy at the major degradation region (around T_{max}) for the as synthesized samples.*

Name of the sample	Maximum degradation temperature (T_{max}) (°C)	Activation energy at the major degradation region (E^d) (KJoule/mole)	Regression factor (R^2)
P0	462	344.68	0.9901
PS5	458	278.58	0.9904
PG5	385	75.98	0.9903

Figure 1a-b

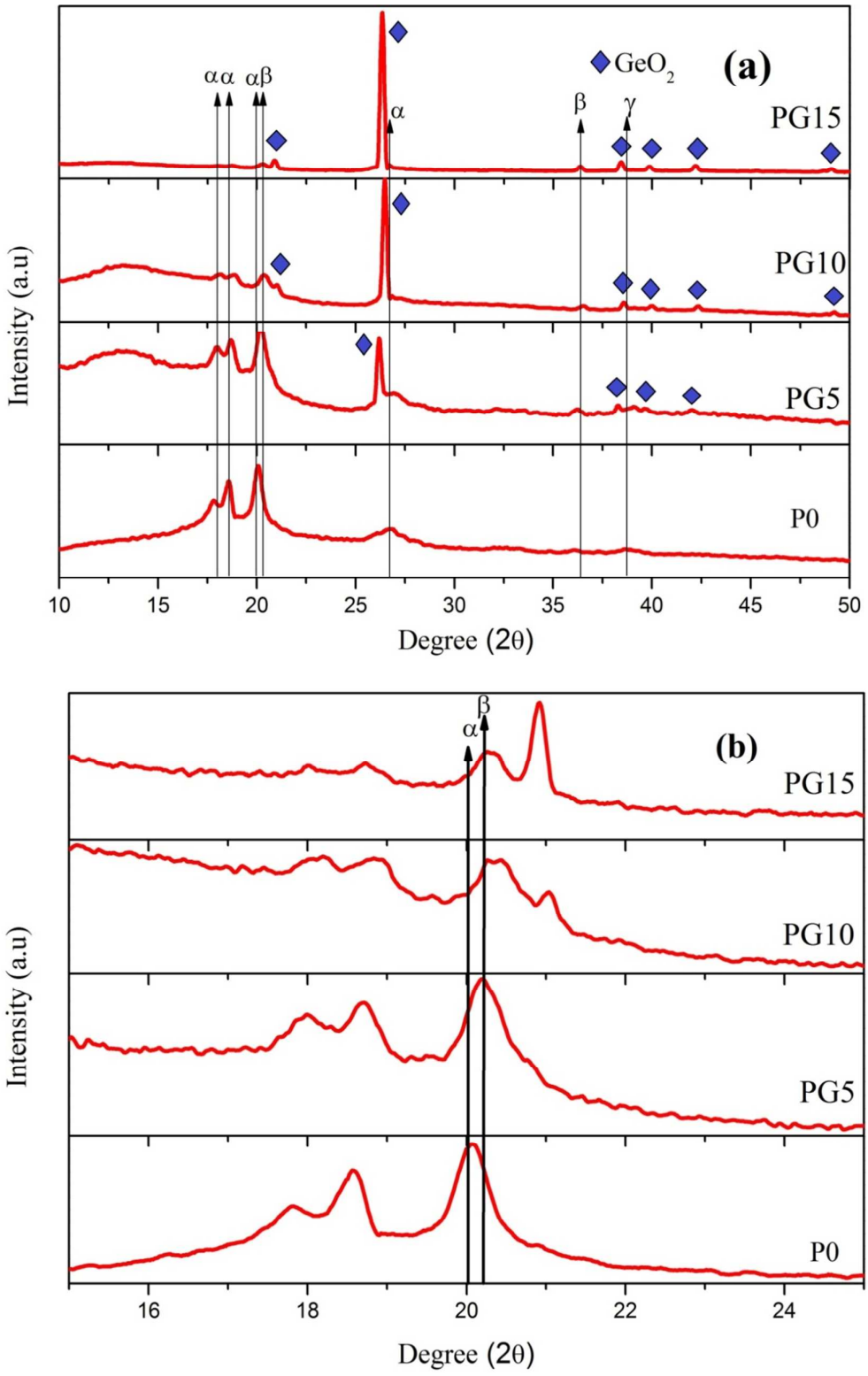

Figure 1: (a) XRD histogram of the samples P0, PG5, PG10 and PG15; (b) Enlarged view of XRD histogram (15˚ to 25˚) of the samples P0, PG5, PG10 and PG15.

Figure 2a-b

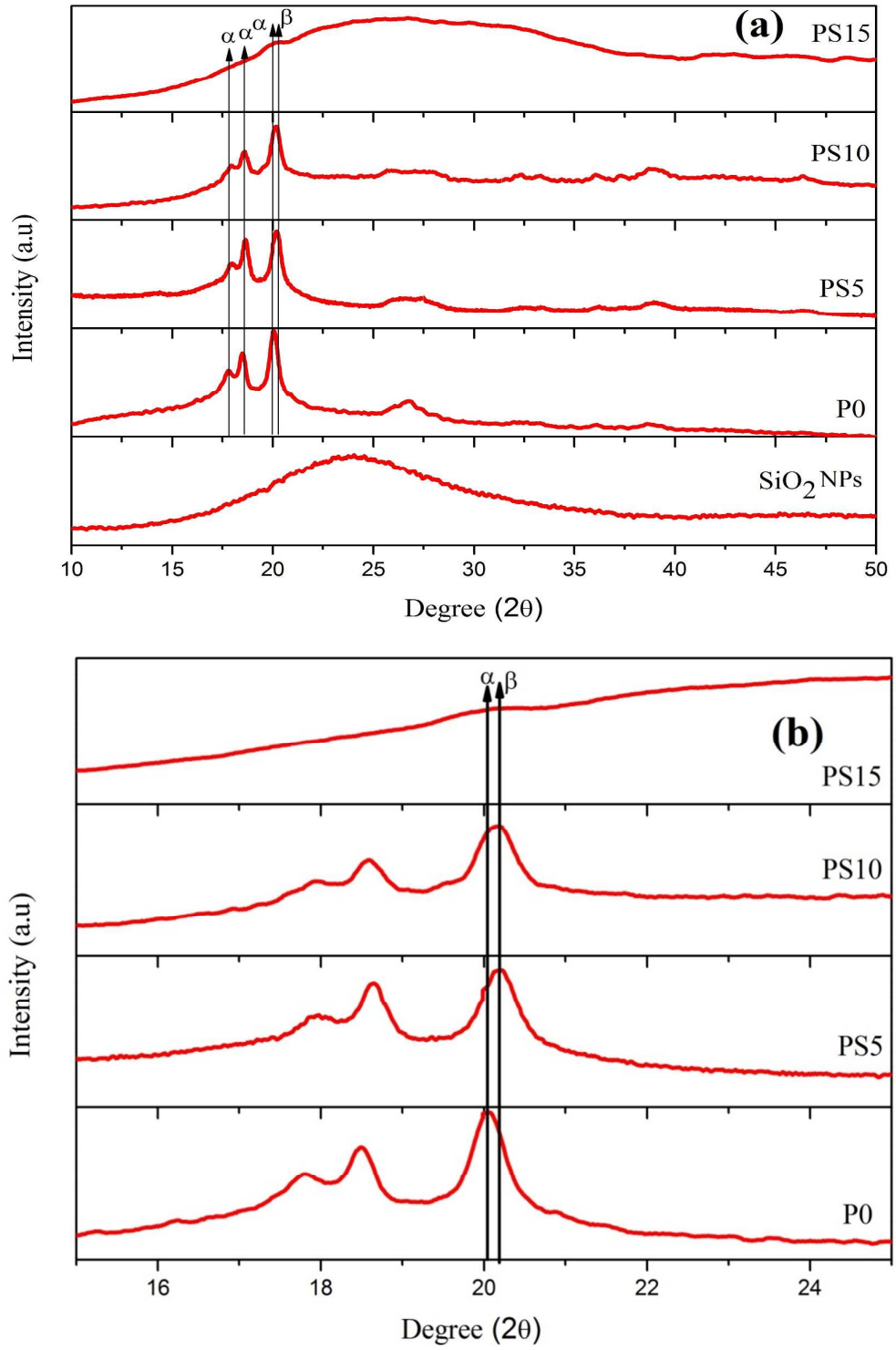

Figure 2: (a) XRD histogram of SiO_2 NPs, P0, PS5, PS10 and PS15; (b) Enlarged view of XRD histogram (15˚ to 25˚) of P0, PS5, PS10 and PS15.

Figure 3a-b

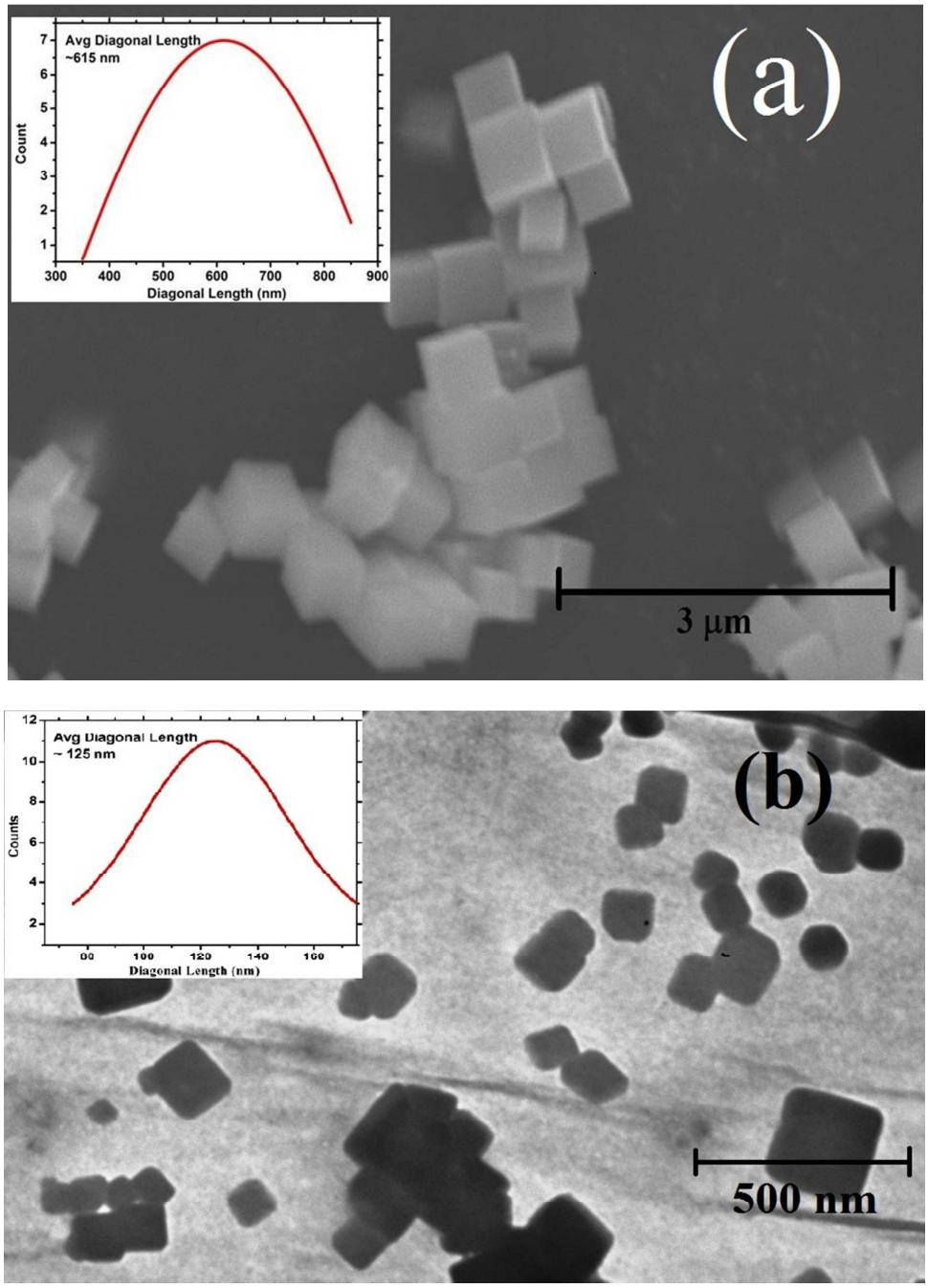

Figure 3: (a) SEM micrograph of as synthesized GeO_2 nanoparticles. Inset shows the size distribution curve of the GeO_2 nanoparticles; (b) TEM micrograph of the GeO_2 nanoparticles. Inset shows the size distribution curve of the GeO_2 nanoparticles.

Figure 4a-b

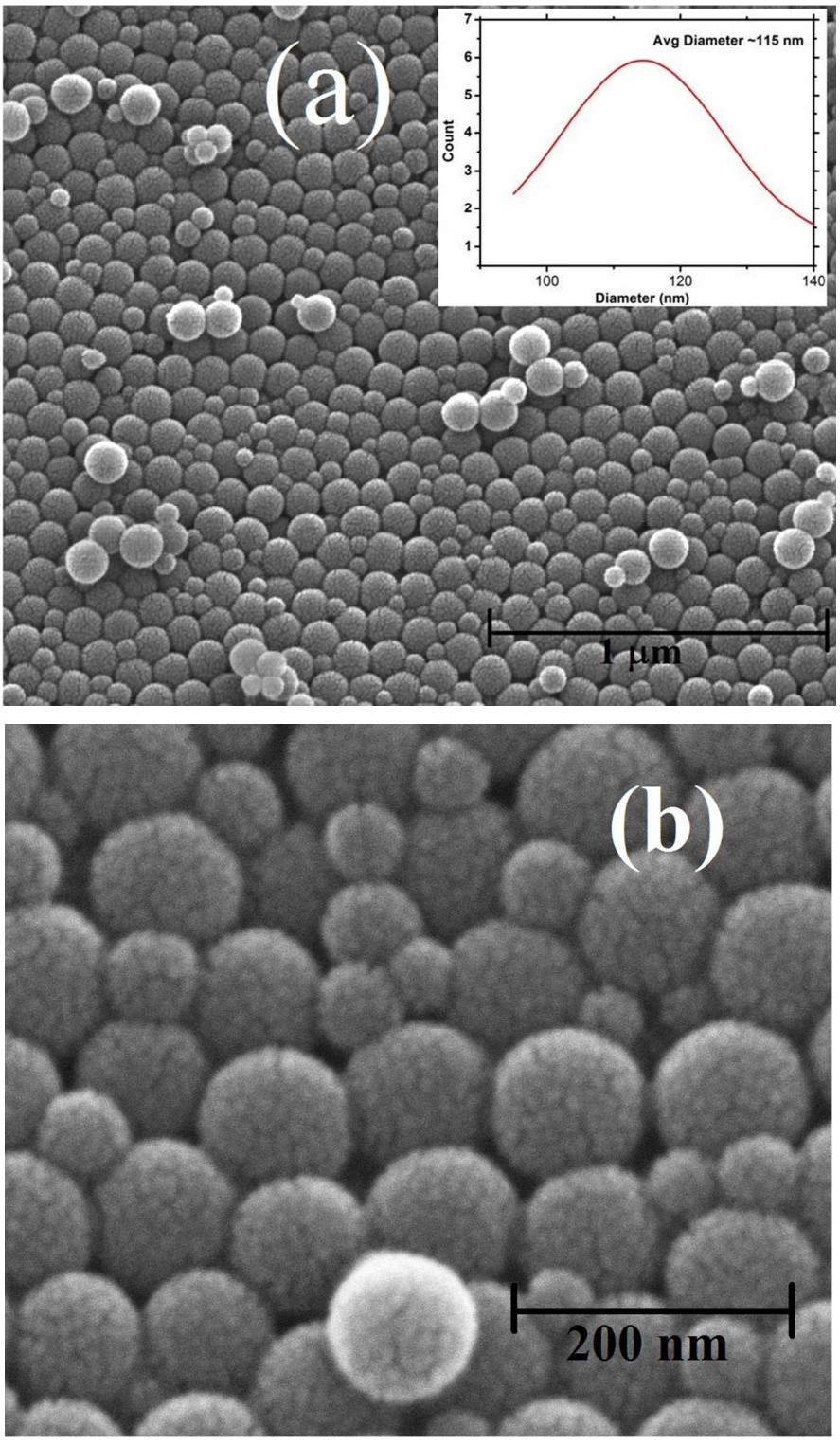

Figure 4c

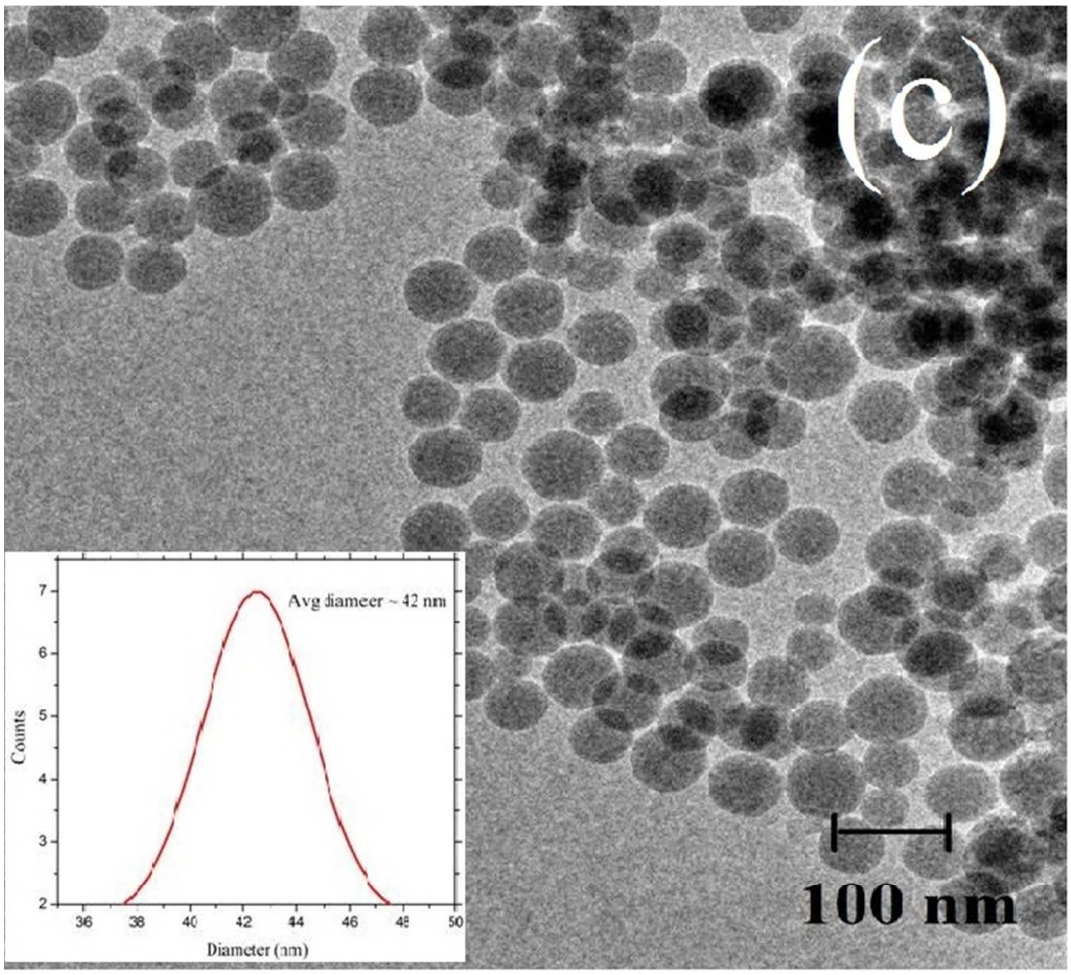

Figure 4: (a) Low magnification FESEM micrograph of SiO_2 nanoparticles. Inset shows the size distribution curve; (b) High magnification FESEM micrograph of as synthesized SiO_2 nanoparticles; (c) TEM micrograph of the SiO_2 nanoparticles. Inset shows the size distribution curve.

Figure 5a-c

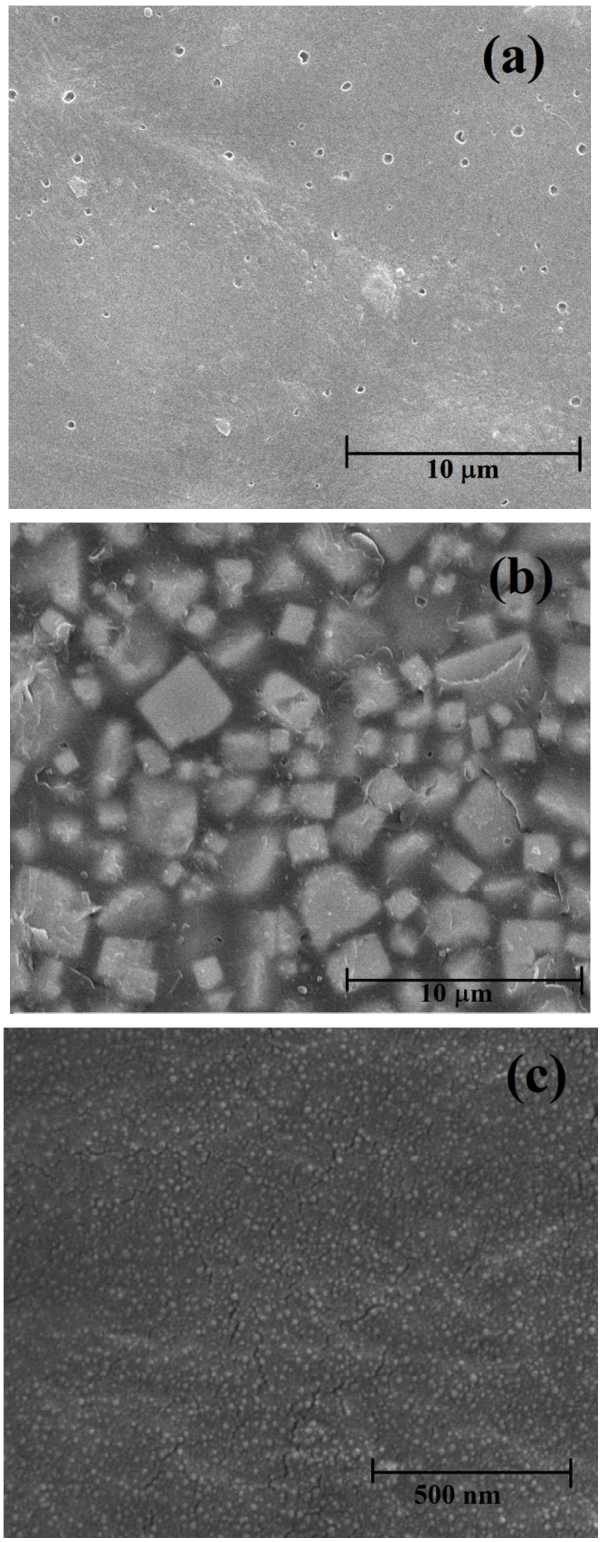

Figure 5: FESEM micrograph of (a) the sample P0; (b) the sample PG15; and (c) the sample PS15.

Figure 6a-b

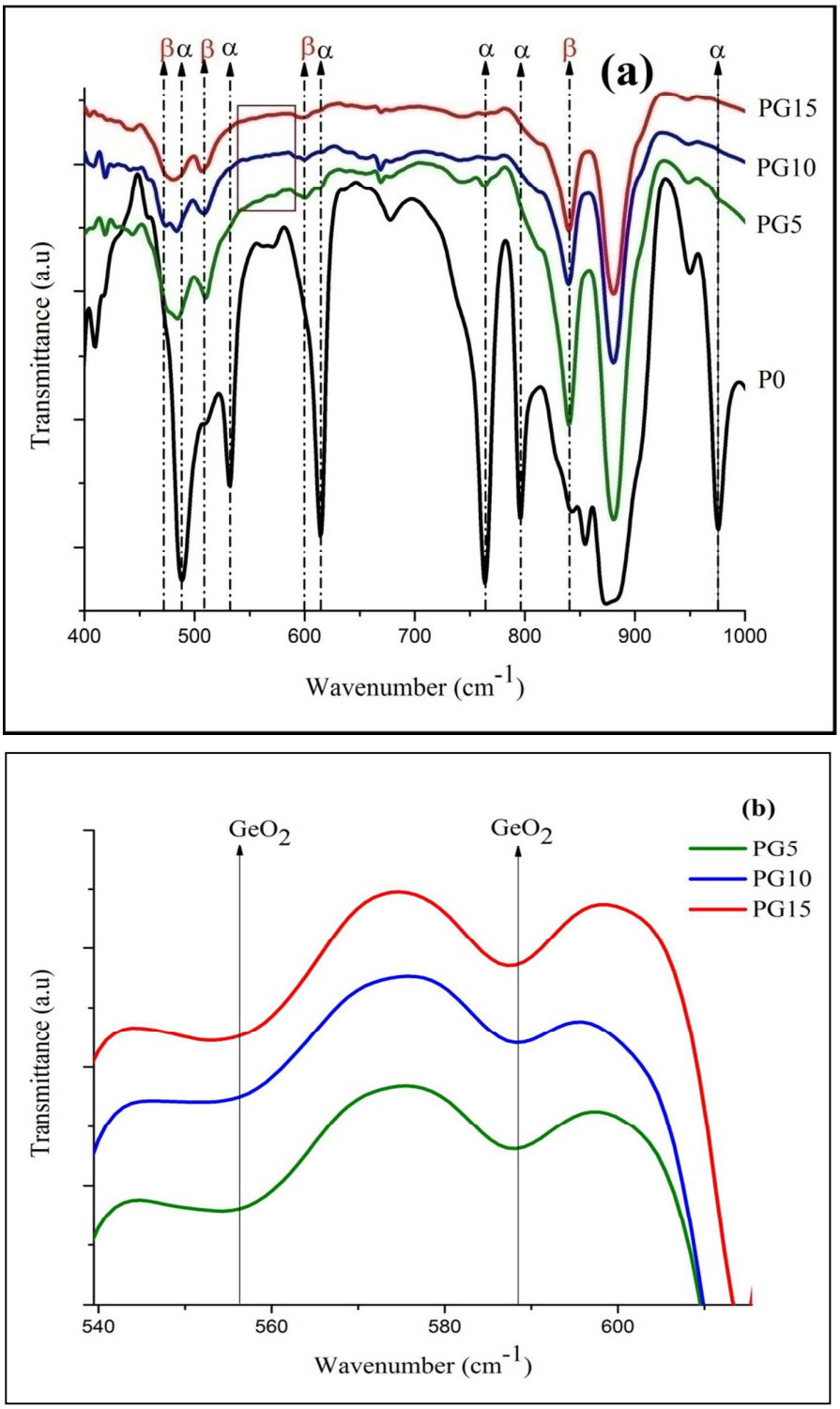

Figure 6: (a) FTIR spectra of the samples P0, PG5, PG10 and PG15; (b) Enlarged view of the marked portion of Fig.6a.

Figure 7

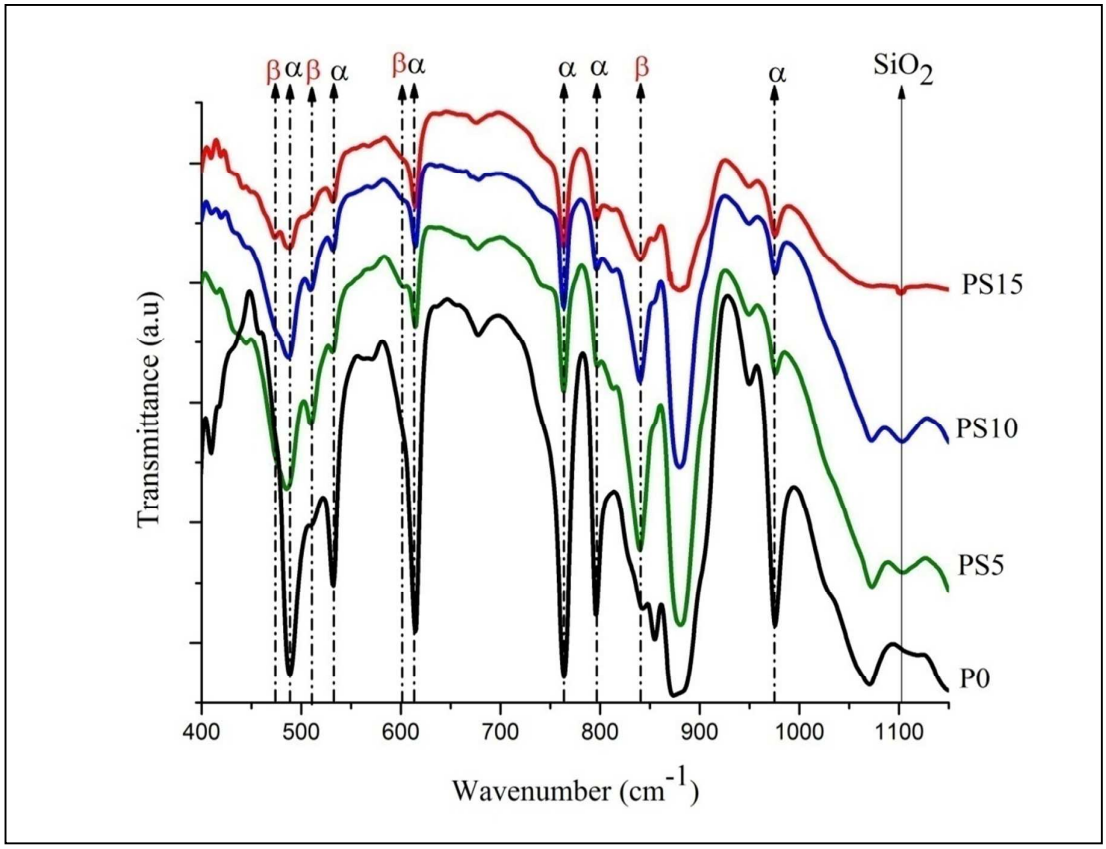

Figure 7: FTIR spectra of the samples P0, PS5, PS10 and PS15.

Figure 8a-b

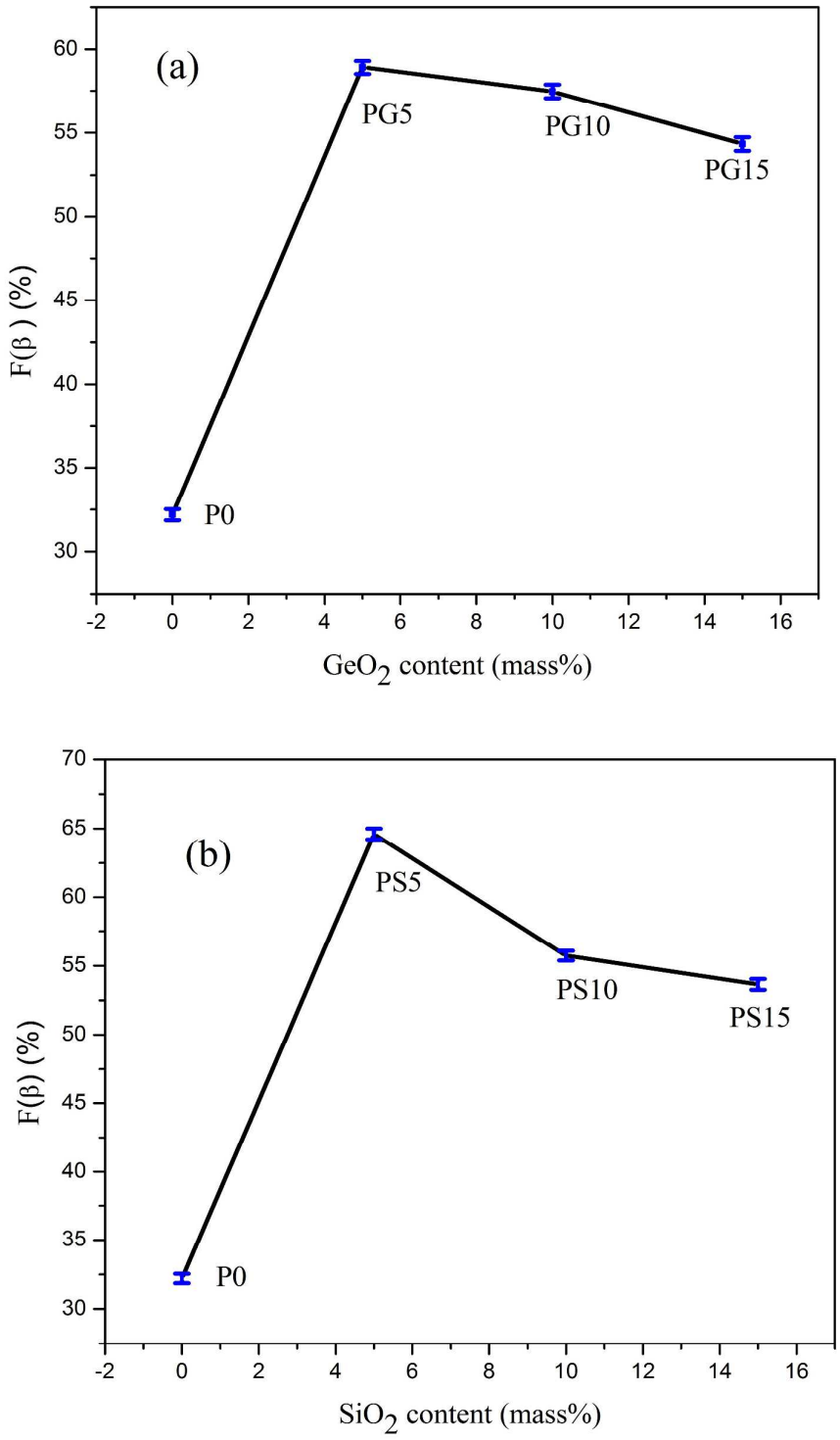

Figure 8: variation of F(β) (β phase fraction) with the filler concentration of (a) GeO_2 nanoparticles; (b) SiO_2 nanoparticles.

Figure 9a-c

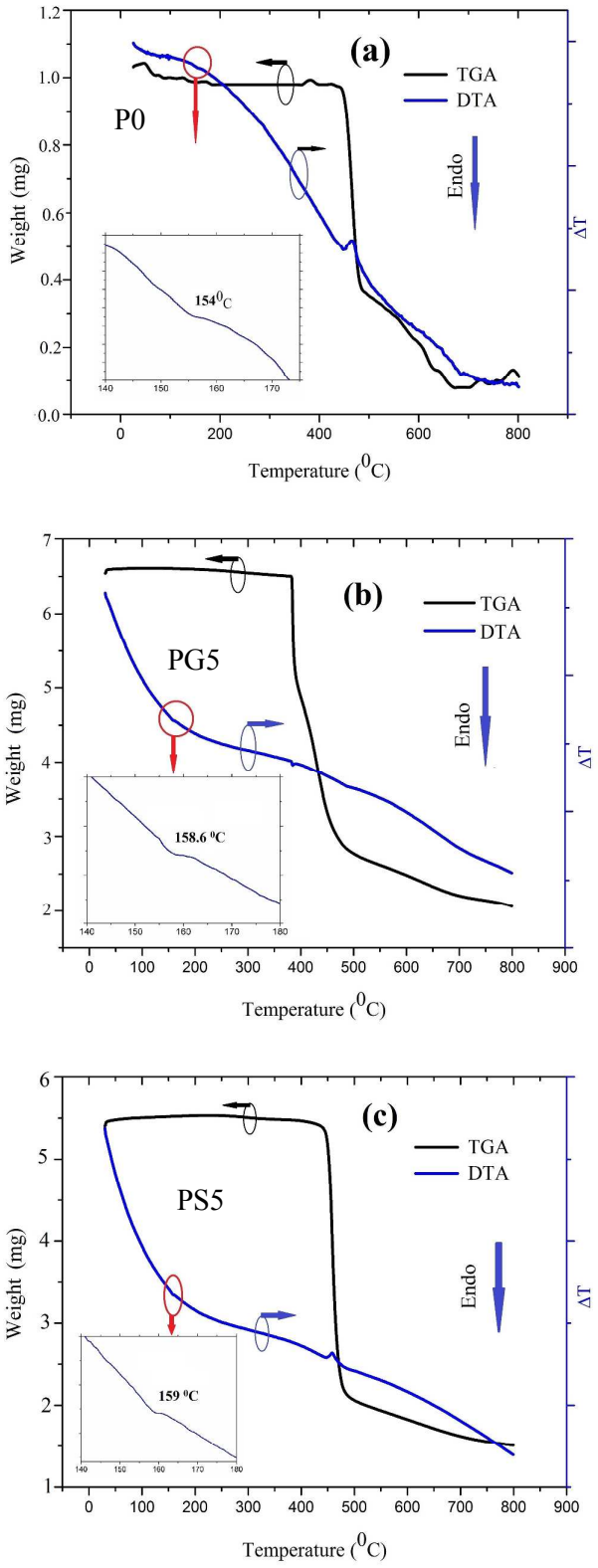

Figure 9: TGA and DTA curve of (a) the sample P0; (b) the sample PG5; and (c) the sample PS5. Insets show the enlarged view of the marked section.

Figure 10

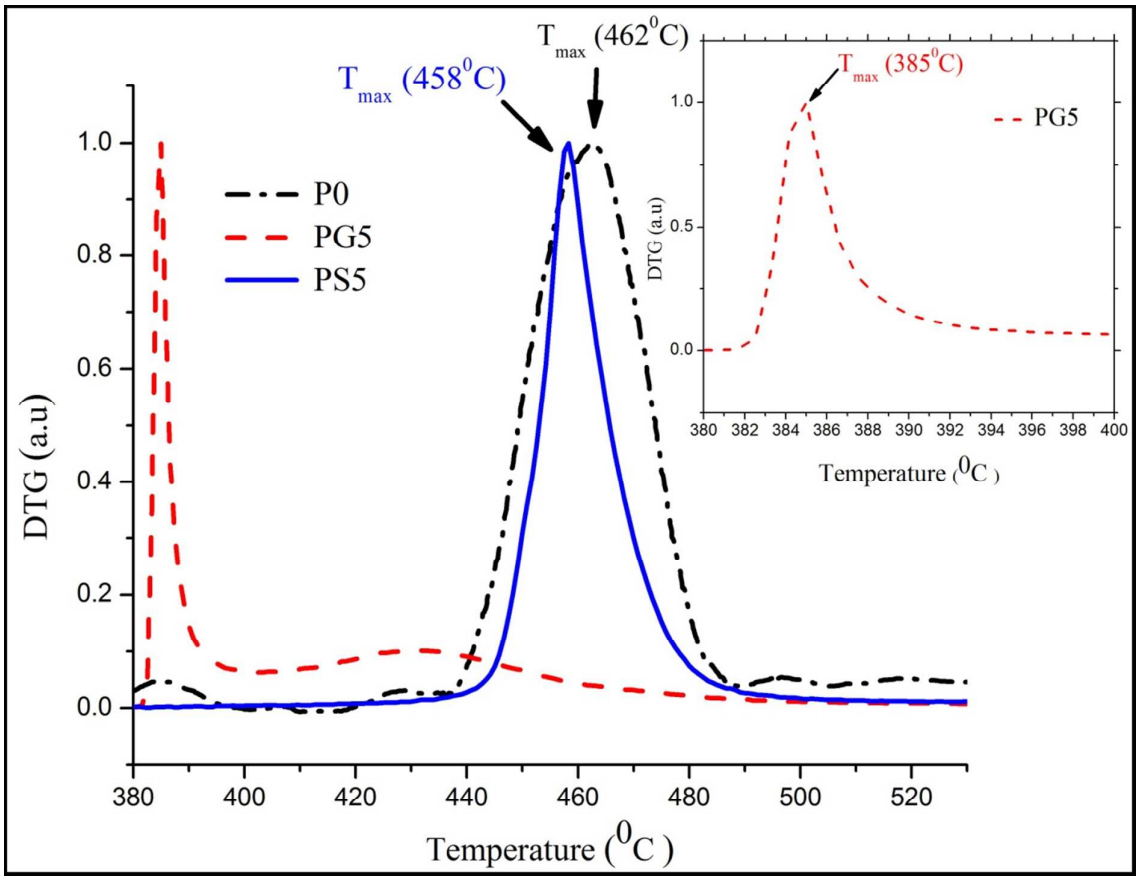

Figure 10: DTG curves of the neat PVDF (P0), PG5 and PS5. Inset shows the enlarged view of DTG curve for the sample PG5.

Figure 11a-c

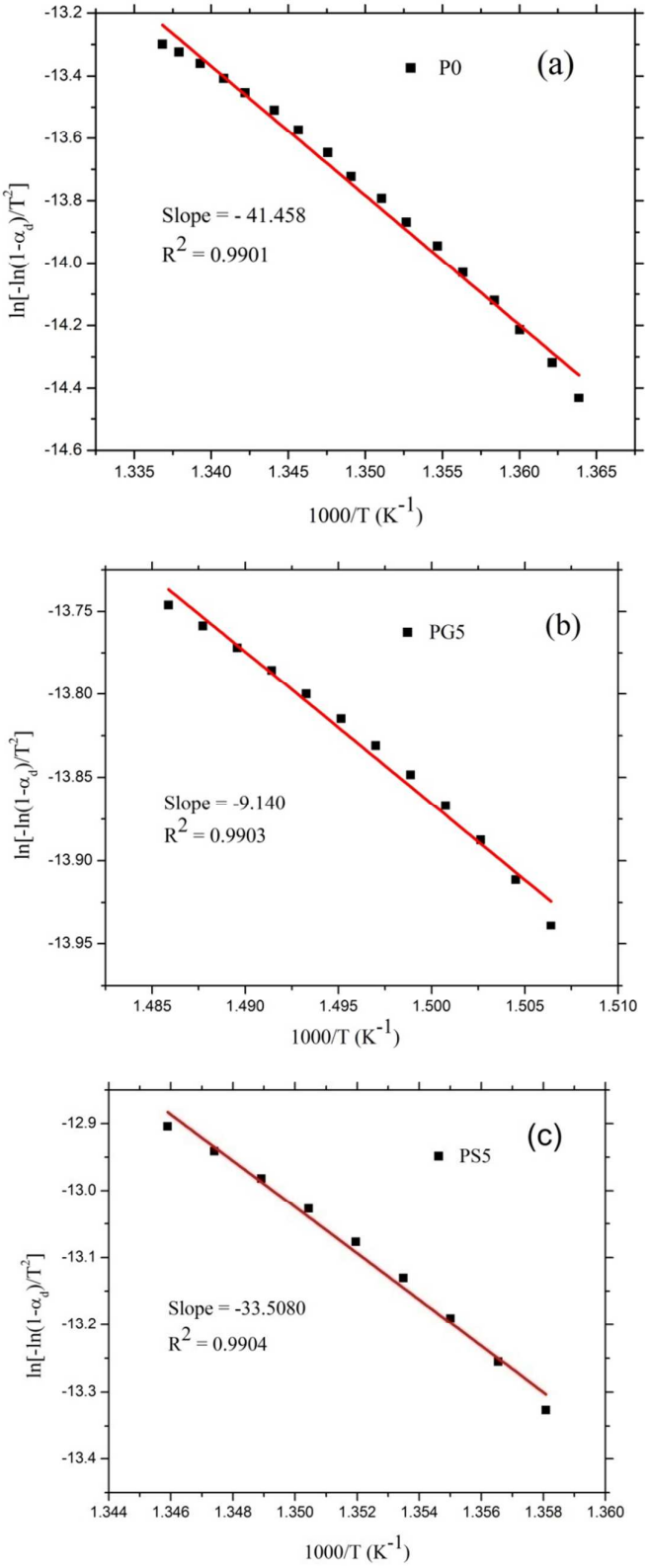

Figure 11: Coats-Redfern plot of (a) P0; (b) PG5; (c) PS5.

Figure 12

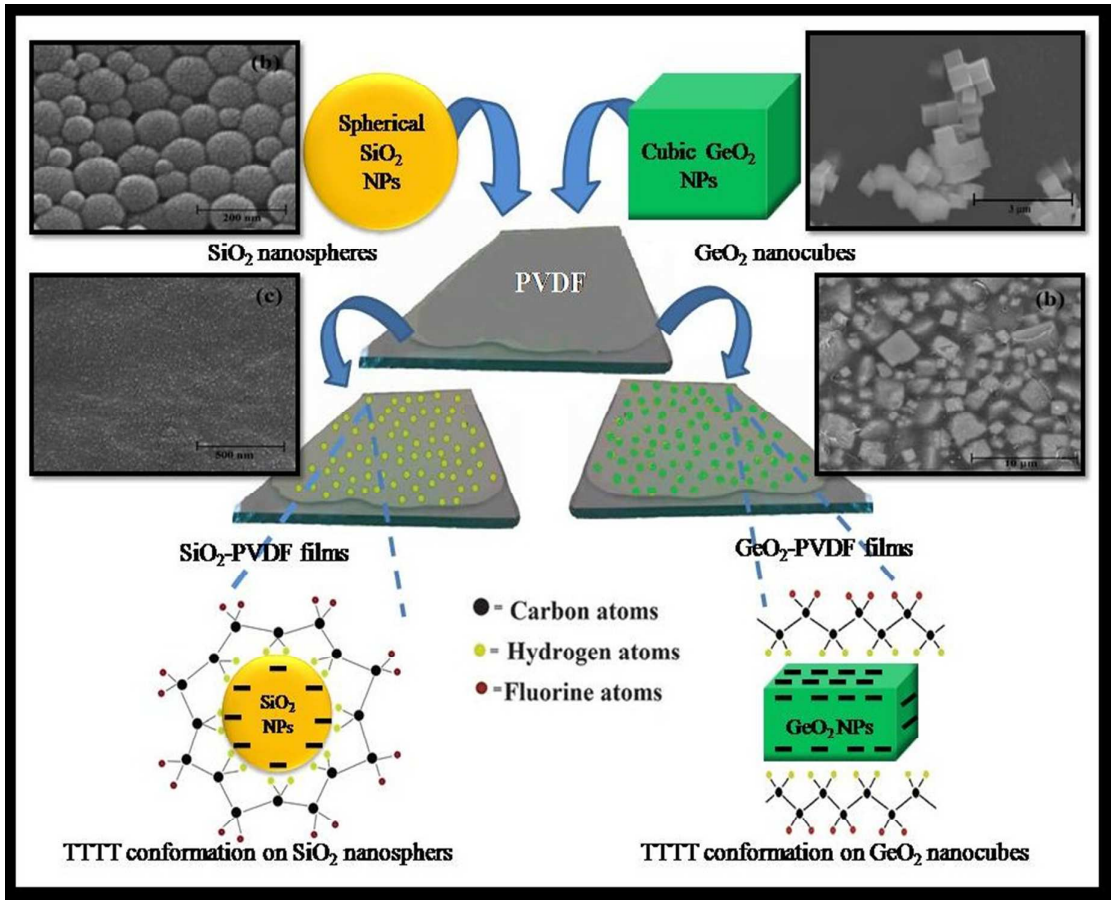

Figure 12: Schematic diagram of the proposed β phase formation mechanism in SPN films.

Figure 13a-c

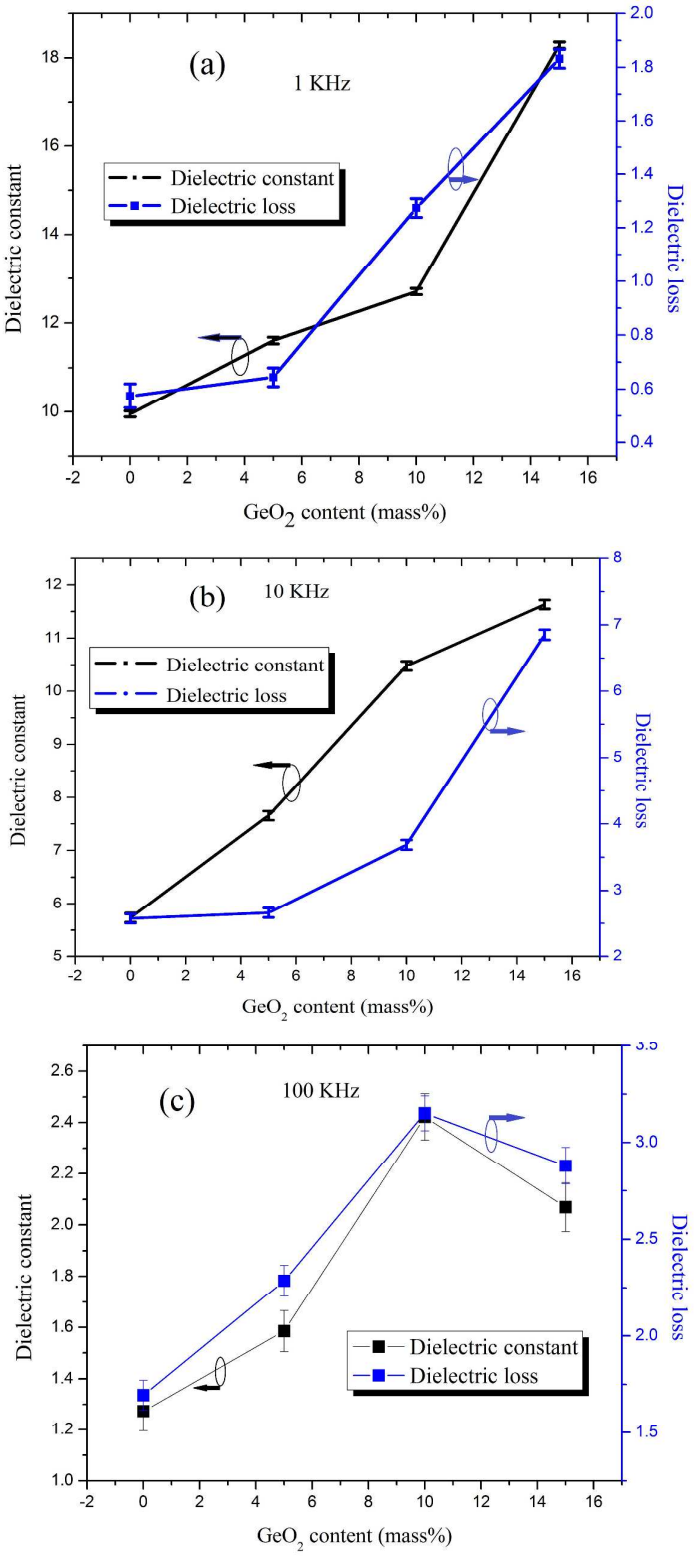

Figure 13: Variation of dielectric constant and dielectric loss with loading concentration (mass%) of GeO_2; at (a) 1 KHz; (b) 10 KHz; and (c) 100 KHz.

Figure: 14a-c

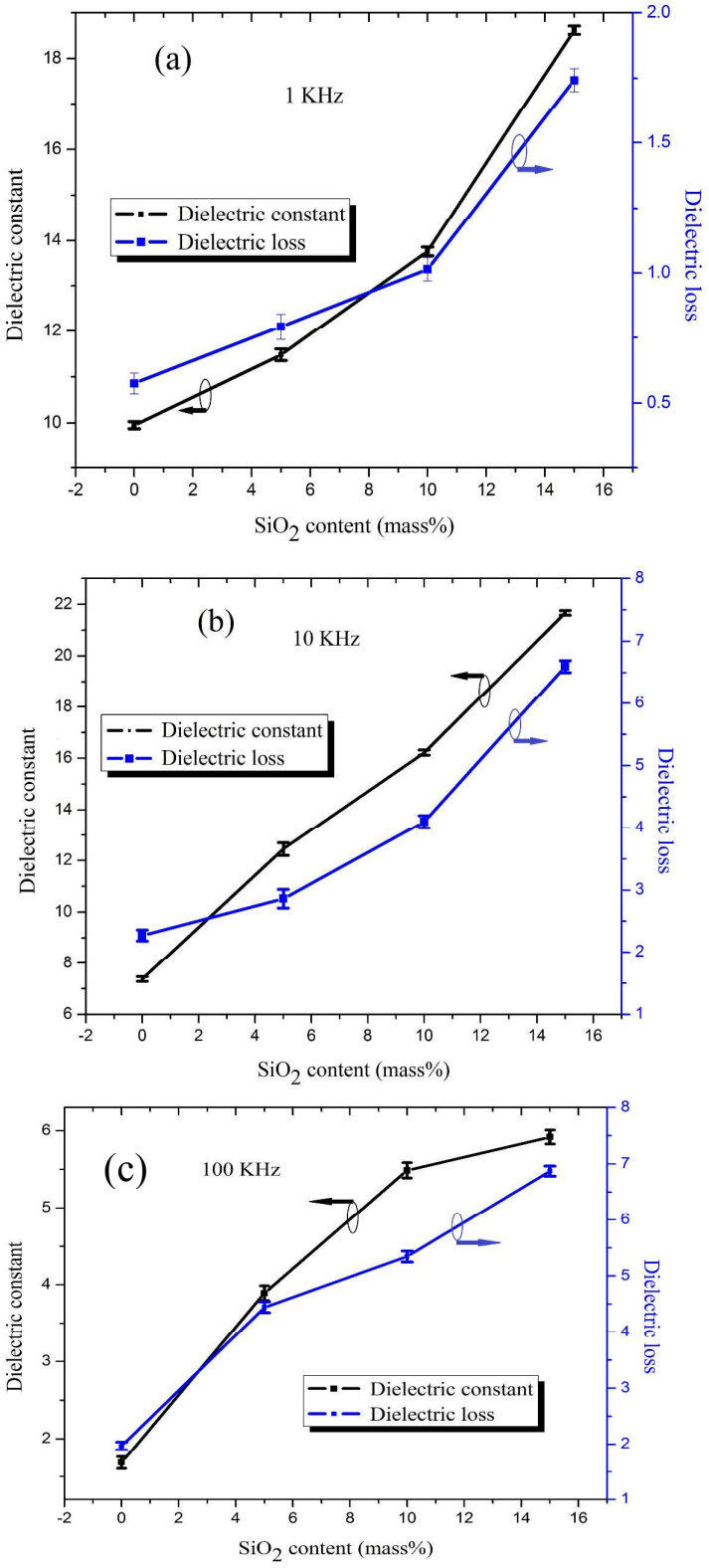

Figure 14: Variation of dielectric constant and dielectric loss with loading concentration (mass%) of SiO_2; at (a) 1 KHz; (b) 10 KHz and (c) 100 KHz.

Figure 15a-b

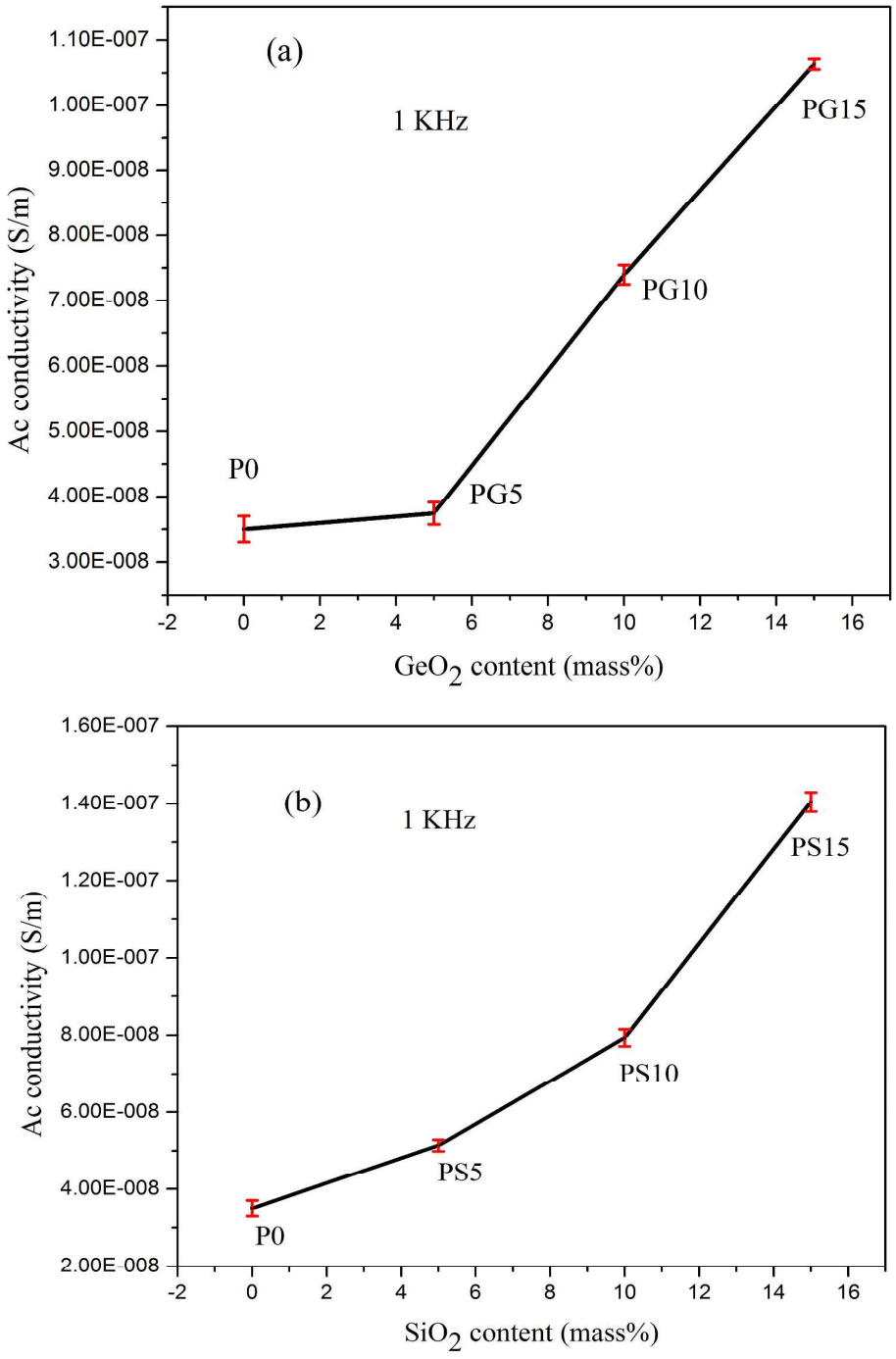

Figure 15: Variation of ac conductivity at 1 KHz with (a) GeO_2 loading percentage (mass%) (b) SiO_2 loading percentage (mass%)

Figure 16a-b

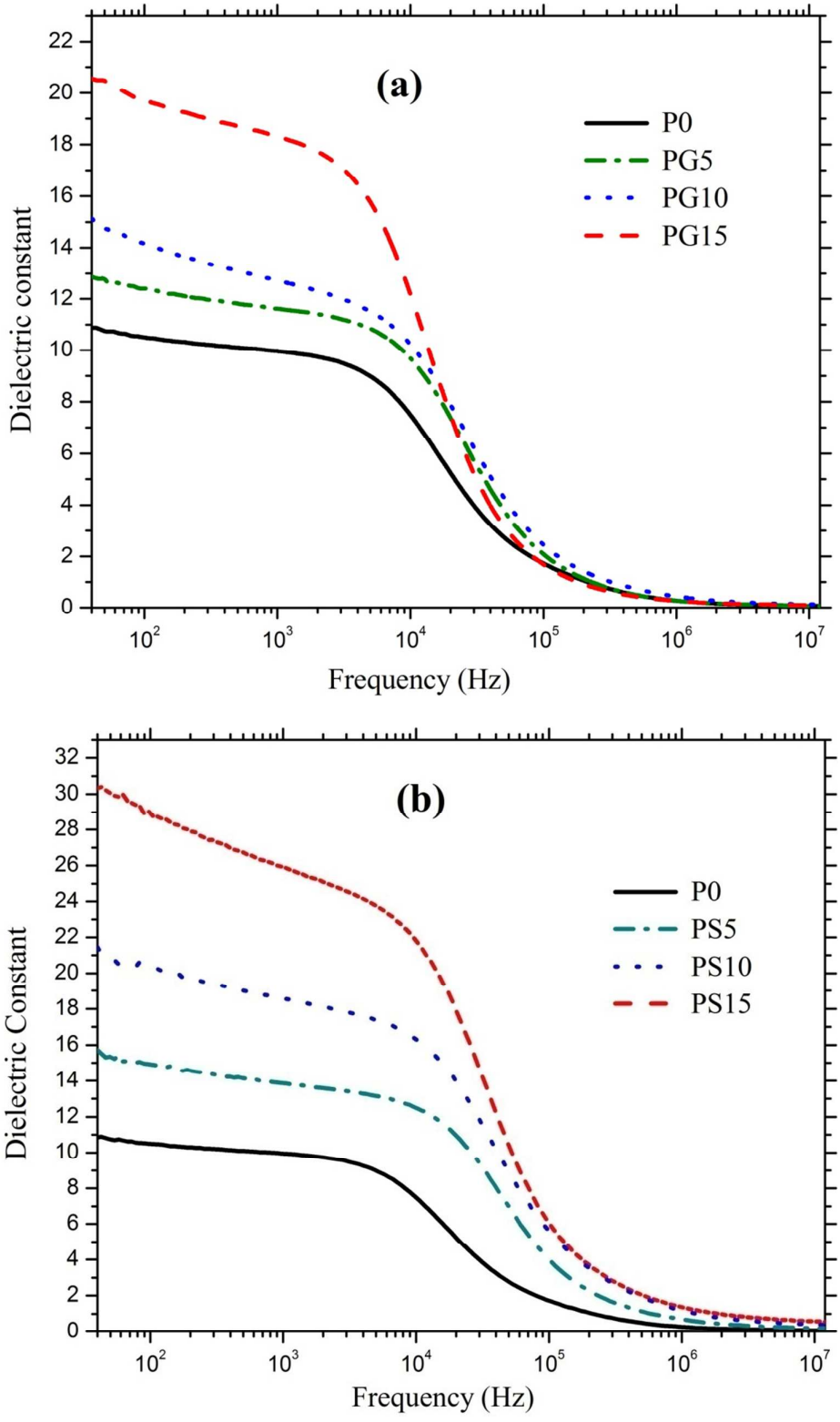

Figure 16: (a) Variation of dielectric constant (ε′) with frequency of (a) the samples P0, PG5, PG10 and PG15; (b) the samples P0, PS5, PS10 and PS15.

Figure 17a-b

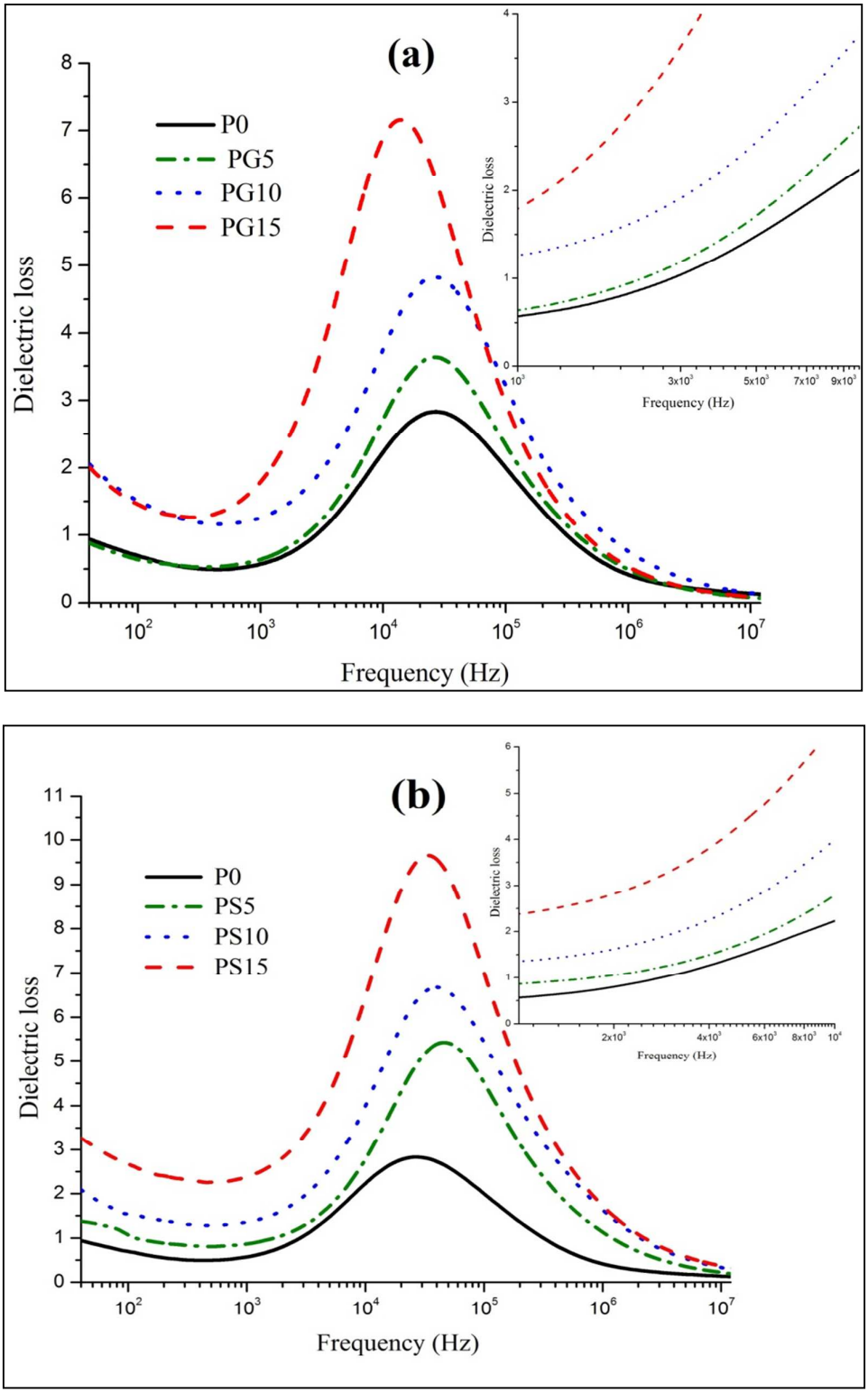

Figure 17: Variation of dielectric loss (ε′′) with frequency of (a) the samples P0, PG5, PG10 and PG15; (b) the samples P0, PS5, PS10 and PS15.

Figure 18a-b

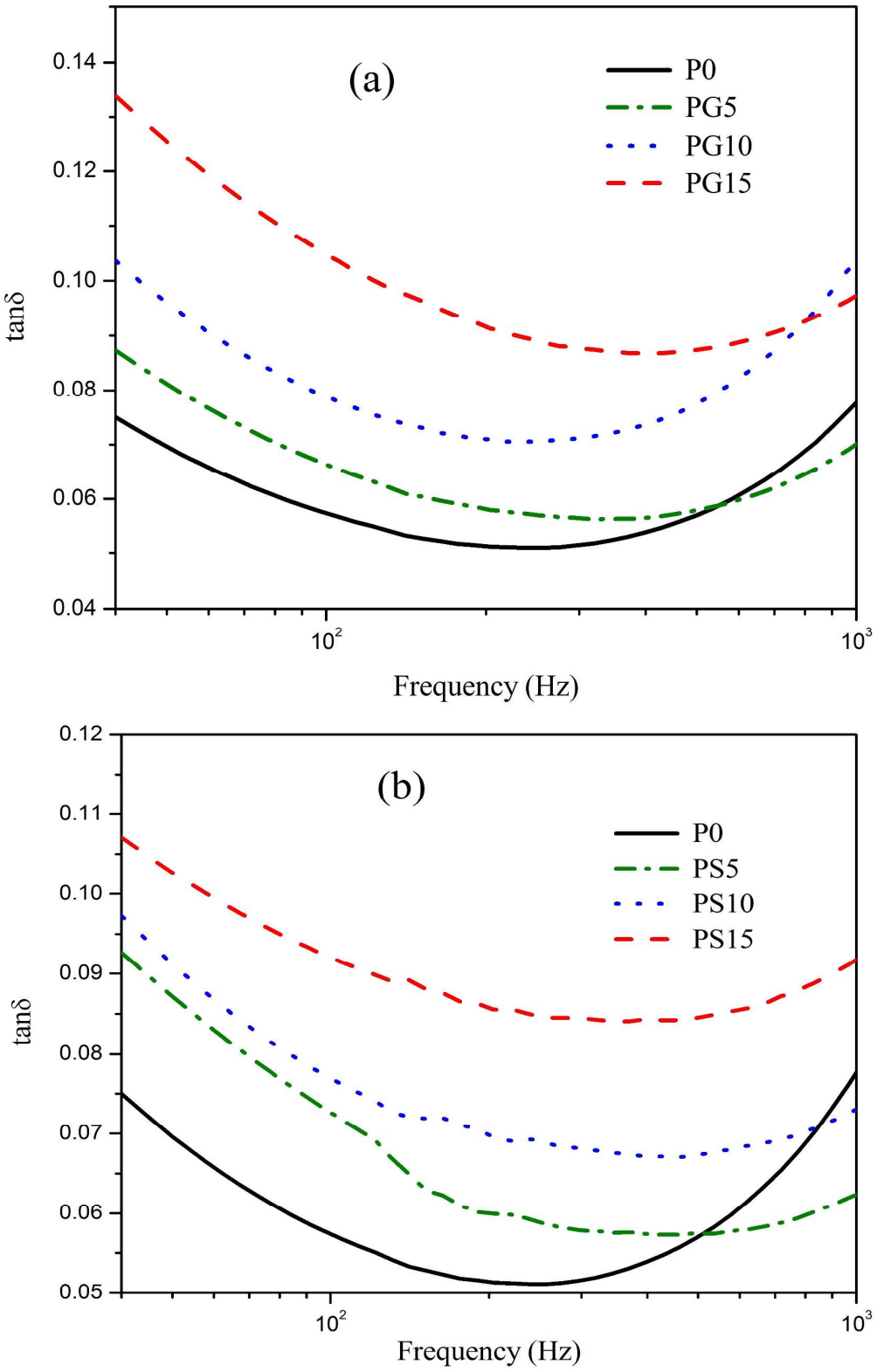

Figure 18. Variation of tanδ with frequency of (a) the samples P0, PG5, PG10 and PG15; (b) the samples P0, PS5, PS10 and PS15

Figure 19a-b

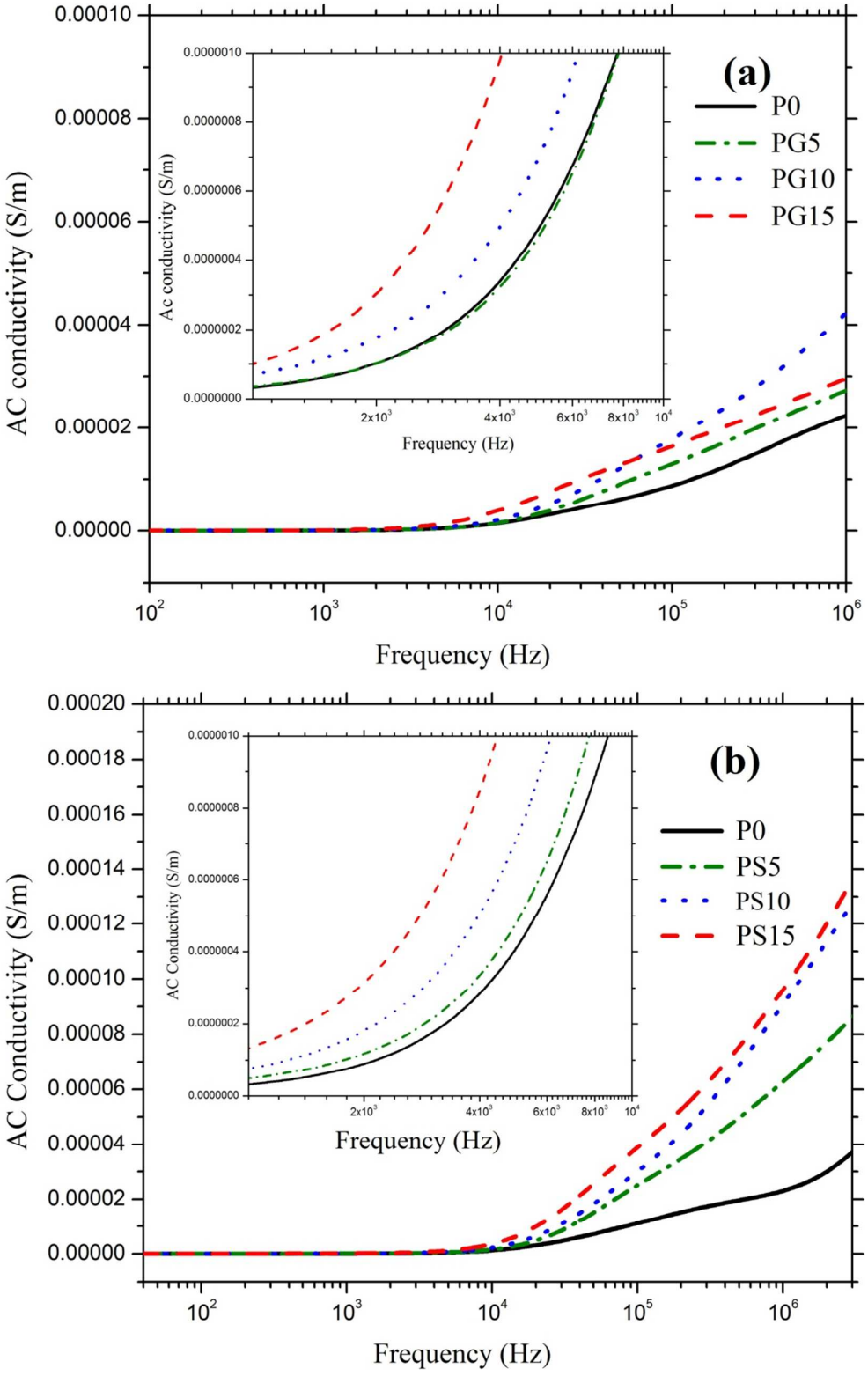

Figure 19: Frequency dependence of ac conductivity for (a) the samples P0, PG5, PG10 and PG15; (b) the samples P0, PS5, PS10 and PS15.